P-TEFb controls cell fate upon p53 activation by modulating intrinsic apoptosis pathway

Zhijia Wang,[1] Andrii Bugai,[1,2,4] Monika Mačáková,[1,4] Caroline C. Friedel,[3] Tina Lenasi,[1] Matjaž Barborič [1,5,*]

[1]Department of Biochemistry and Developmental Biology, University of Helsinki, Helsinki FIN-00014, Finland

[2]Department of Molecular Biology and Genetics, Aarhus University, 8000 Aarhus C, Denmark

[3]Institute for Informatics, Ludwig-Maximilians-Universität München, 80333 Munich, Germany

[4]These authors contributed equally

[5]Lead contact

[*]Correspondence: matjaz.barboric@helsinki.fi

SUMMARY

Positive transcription elongation factor b (P-TEFb) is the crucial player in RNA polymerase II (Pol II) pause release that has emerged as a potential target for many types of cancer. Because single-agent therapies are bound to fail in delivering durable clinical response, targeting of P-TEFb shall benefit when deployed as a combination therapy. By conducting a functional screen with a comprehensive oncology library, we identify clinically relevant antimetabolites and Mouse double minute 2 homolog (MDM2) inhibitors as top classes of compounds that induce p53-dependent death of colon cancer-derived cells in synergy with selective inhibitors of P-TEFb. While targeting of P-TEFb augments apoptosis triggered by the genotoxic antimetabolite 5-fluorouracil, it switches the fate of cancer cells enacted by the non-genotoxic MDM2 inhibitor Nutlin-3a from cell-cycle arrest to apoptosis. Importantly, we uncover that execution of the intrinsic apoptosis pathway characterizes the cell fate switching, which is driven by induction of p53-dependent pro-apoptotic genes and concurrent repression of P-TEFb-dependent pro-survival genes, including those encoding key components of the oncogenic PI3K-AKT pathway. Finally, we show that the combination treatments remain effectual in a three-dimensional (3D) cell culture setting, suggesting a translational potential of our work.

INTRODUCTION

Gene transcription by RNA polymerase II (Pol II) is a highly regulated process that determines levels of gene expression and, by extension, nearly all facets of cellular identity, fate, and metabolism. A central regulatory hub is the carboxy-terminal domain (CTD) of the largest subunit of Pol II, RPB1, which comprises heptad repeats with the consensus sequence $Tyr^1Ser^2Pro^3Thr^4Ser^5Pro^6Ser^7$ (Eick and Geyer, 2013). During the transcription cycle, multiple positions within the CTD repeats are subject to dynamic phosphorylation and dephosphorylation events by transcriptional cyclin-dependent kinases (tCDKs) and phosphatases, respectively. These post-translational modifications modulate the binding of factors required for precursor mRNA (pre-mRNA) initiation, elongation, cotranscriptional maturation, and termination, as well as chromatin modification (Bentley, 2014; Parua and Fisher, 2020).

Initiation of transcription is stimulated by CDK7, which is together with its regulatory partners cyclin H and Mat1 recruited to the Mediator-Pol II pre-initiation complex on gene promoters to phosphorylate Ser5 and Ser7 residues of the CTD. Concurrently, CDK7 promotes 5′-end capping of transcripts and facilitates promoter-proximal pausing of Pol II by stimulating the recruitment of DRB-sensitivity inducing factor (DSIF) and negative elongation factor (NELF), which bind and arrest Pol II in an inactive conformation (Parua and Fisher, 2020; Vos et al., 2018b). Critically, the release of paused Pol II into elongation genome-wide is triggered by the positive transcription elongation factor b (P-TEFb), composed of the catalytic CDK9 and a regulatory cyclin T1 or T2 subunit (Core and Adelman, 2019; Zhou et al., 2012). P-TEFb phosphorylates Ser2 residues across the CTD and its linker, as well as multiple positions within both pause-inducing factors, converting DSIF into a positive elongation factor and triggering dissociation of NELF from Pol II. In turn, the polymerase associated factor complex (PAFc) binds Pol II while SPT6 docks to the CTD linker region, allowing Pol II elongation to resume (Vos et al., 2018a). Adding another layer of complexity, the P-TEFb-driven release of Pol II into elongation is opposed by phosphoprotein phosphatases, such as a protein phosphatase 2A (PP2A) complex, which is recruited to Pol II by the Integrator complex to antagonize phosphorylation of key P-TEFb substrates including DSIF and the Pol II CTD (Cossa et al., 2021; Huang et al., 2020; Vervoort et al., 2021). Upon the release of Pol II from pausing, the homologous CDK12 and CDK13 interact with cyclin K to stimulate Pol II elongation throughout gene bodies and facilitate production of full-length transcripts through suppressing their premature cleavage and polyadenylation (Blazek et al., 2011; Krajewska et al., 2019). Finally, while CDK8 and its CDK19 paralogue bind cyclin C to influence gene expression by phosphorylating transcription factors and controlling Mediator structure and function (Luyties and Taatjes, 2022), the little studied CDK11 binds cyclins L1 and L2 to phosphorylate the CTD Ser2 residues for efficient elongation and 3’ end processing of replication-dependent histone gene transcripts (Gajdušková et al., 2020).

Historically, transcription by Pol II has been deemed too essential to healthy cells for being considered as a target in cancer. Intriguingly, recent work shows that genetic and epigenetic alterations of cancer cells drive a transcriptionally deregulated state, referred to as transcriptional addiction, which facilitates tumor initiation and progression (Bradner et al., 2017; Vervoort et al., 2022). Correspondingly, the addiction, while absent in non-cancerous cells, may instigate a disproportionate reliance on core components of the Pol II machinery to support tumor growth and survival, rendering cancer cells sensitive to perturbation of discrete phases of the transcription cycle (Parua and Fisher, 2020; Vervoort et al., 2022). Indeed, recent work demonstrated that targeting CDK7, CDK9, and CDK12 with selective and potent small-molecule inhibitors could lead to vigorous anti-tumor effects in xenograft and pre-clinical cancer models (Minzel et al., 2018; Quereda et al., 2019; Wang et al., 2015; Zhang et al., 2018), conceivably because of heightened demand for specific tCDKs in sustaining high-level transcription of pro-survival genes and/or oncogene-driven gene expression programs in rapidly dividing cancer cells. Importantly, while effective, the inhibitors of tCDKs imposed minimal toxicity to normal tissues. This is an important improvement over preclinical

studies and/or clinical trials with pioneering pan-CDK inhibitors such as flavopiridol, which produced undesirable side effects including particularly concerning blood toxicities like neutropenia (Morales and Giordano, 2016).

Despite hopeful prospects for targeting tCDKs in cancer, single-agent tCDK interventions may fail to culminate in durable responses due to therapeutic adaptation and/or presence of pre-existing tumor clones refractory to the therapy (Boshuizen and Peeper, 2020). Hence, tCDK-centered anti-cancer strategies should benefit when deployed as part of combination therapies, which shall also enable compounds to be used at lower doses than as single agents, thus offsetting a potential for undesirable toxicities associated with a particular compound. Furthermore, while single-agent therapies could lead to reversible cytostatic responses, combination approaches might trigger irreversible cell death, the desirable outcome of any effective cancer treatment.

In this study, we began addressing this issue by targeting P-TEFb, the crucial player in Pol II pause release that has emerged as a potential drug target for many types of cancer (Galbraith et al., 2019; Vervoort et al., 2022). We screened a comprehensive library of oncology compounds to identify those that would be lethal for our model colon cancer-derived cell line in combination with NVP-2, a highly selective inhibitor of P-TEFb that effectuates a potent anti-cancer activity at non-toxic doses (Li et al., 2022; Olson et al., 2018). This effort led to the identification of several clinically relevant groups of compounds, including antimetabolites and Mouse double minute 2 homolog (MDM2) inhibitors, for which we show that they elicit synthetic lethality together with selective antagonists of P-TEFb in p53-dependent manner. We paid special attention to the pioneering MDM2 inhibitor Nutlin-3a, which is a non-genotoxic protein–protein interaction (PPI) inhibitor that reactivates the tumor suppressor p53 by dislodging it from its cognate E3 ubiquitin ligase MDM2 and thus promises to be a powerful anti-cancer agent for patients with wild-type (WT) p53 (Vassilev et al., 2004). We show that selective perturbation of P-TEFb converts the fate of Nutlin-3a-treated cells from cell-cycle arrest to apoptosis in p53-dependent fashion. Moreover, we uncover that the synthetic lethality of p53 activation and P-TEFb inhibition (PAPI) is driven by induction of p53-dependent pro-apoptotic genes and concurrent repression of P-TEFb-dependent pro-survival genes encoding key components of an oncogenic PI3K-AKT pathway. Finally, we show that combination treatments within the PAPI framework remain effective in a three-dimensional (3D) cell culture setting, highlighting the translational potential of our work.

RESULTS

An oncology library screen identifies MDM2 inhibitors and antimetabolites as top compound classes that are synthetic-lethal with selective P-TEFb inhibitor NVP-2

To identify potentially therapeutic compounds that would elicit synthetic lethality in combination with highly selective inhibitor of P-TEFb, we conducted an oncology library screen using HCT116 cell line, a well-established model of colorectal cancer encoding the oncogenic $KRAS^{G13D}$ and $PIK3CA^{H1047R}$ proteins (Figure 1A). We employed FO5A oncology library consisting of 528 investigational and clinical anti-cancer compounds (Figure S1A), and NVP-2, an aminopyrimidine-derived ATP-competitive inhibitor of P-TEFb. We chose NVP-2 over other P-TEFb antagonists due to its superb potency and selectivity. Namely, NVP-2 inhibits the P-TEFb catalytic activity and Ser2 phosphorylation of RNA Pol II with half maximal inhibitory concentration [IC_{50}] values of 0.5 nM and 4 nM, respectively, and displays at least 1,200-fold lower activity toward CDK1, 2, 4, and 7 (Olson et al., 2018). To determine the dose of NVP-2 used in the screen, we exposed HCT116 cells to increasing concentrations of NVP-2 and measured cellular viability with luminescence-based assay in which the number of metabolically active cells is determined by quantifying the levels of ATP via luciferase reaction. This approach revealed the IC_{50} value of NVP-2 in HCT116 was 4 nM (data not shown). As we aimed to identify compounds eliciting synergistic cell killing in combination with NVP-2, we elected to use 3 nM of NVP-2, which corresponded to its IC_{30} dose.

We dispensed DMSO- and NVP-2-treated HCT116 cells robotically to 384-well plates containing the FO5A library compounds at five ten-fold serial dilutions, cultured them for 72 hours, upon which we measured cellular response to the library compounds using fluorescence-based cytotoxicity assay, in which compromised membrane integrity of dead cells is proportional to fluorescence signal generated by the binding of an otherwise cell impermeable cyanine dye to DNA. To quantify cytotoxicity elicited by the treatments, we generated dose-response curves at each compound concentration and used these to calculate drug sensitivity score (DSS), an area under the dose–response curve type metric as described previously (Yadav et al., 2014a). Finally, we calculated differential DSS (dDSS) values by comparing response to the library compounds in the presence and absence of NVP-2. Combination treatments of the library compounds and NVP-2 with dDSS value above 5 were considered effective. This analysis identified 52 compounds, of which top seven groups include antimetabolites (n = 7), Mouse double minute 2 homolog (MDM2) inhibitors (n = 4), PARP inhibitors (n = 4), Inhibitor of apoptosis (IAP) inhibitors (n = 3), farnesyl transferase inhibitors (n = 2), Aurora kinase inhibitors (n = 2) and Bromodomain and Extra-Terminal Domain (BET) inhibitor/degrader (n = 2) (Figures 1B and S1B).

Amongst transcriptional CDKs, selective targeting of P-TEFb shows the most synergistic lethality with MDM2 inhibitors and antimetabolites

A common denominator of two top compound groups of our screen is activation of p53. While the identified antimetabolites are used as chemotherapeutics for a variety of cancers, clinical trials with MDM2 inhibitors have had only a limited success thus far (Konopleva et al., 2020). Nevertheless, the long-standing quest in delivering these inhibitors into the clinic continues, particularly in the context of MDM2 combination therapies. Hence, in this study we investigated how MDM2 inhibitors and antimetabolites elicit synthetic lethality with selective targeting of P-TEFb. As representative compounds, we employed a pioneering MDM2 inhibitor Nutlin-3a and an antimetabolite fluoropyrimidine 5-fluorouracil (5-FU) throughout our work. Whereas Nutlin-3a acts as a competitive PPI inhibitor of the p53-MDM2 interface by mimicking three hydrophobic amino acid residues of p53 required for MDM2 binding (Vassilev et al., 2004), metabolites of 5-FU interfere with cellular

metabolism via incorporating into RNA and DNA and inhibiting the nucleotide synthetic enzyme thymidylate synthase (Longley et al., 2003). Even though both compounds activate the p53 pathway in HCT116 cells, non-genotoxic Nutlin-3a triggers reversible cell-cycle arrest in p53-dependent fashion (Tovar et al., 2006), while genotoxic 5-FU elicits rapid p53-dependent apoptosis (Bunz et al., 1999).

To independently confirm the screen results that MDM2 inhibitors and antimetabolites sensitize HCT116 cells to P-TEFb antagonists and to test for synergy of the combination treatments, we first conducted cytotoxicity assays with combinatorial titrations of Nutlin-3a with NVP-2. Whereas Nutlin-3a alone did not show any cytotoxicity across the tested concentrations, it became highly toxic in the presence of sub-lethal doses of NVP-2 (Figure 1C). Of note, cellular response to NVP-2 alone was biphasic, suggesting that transcriptional shutdown at high NVP-2 doses is incompatible with cell death. We next determined Bliss synergy scores for all combinations (Ianevski et al., 2020). Here, the Bliss score is a readout for synergy depicting the difference between expected effect, which assumes the additive contribution of individual treatments, and observed effect, with positive scores indicating synergy of combination treatment. This analysis showed a striking degree of synergy between high doses of Nutlin-3a and low doses of NVP-2 in inducing lethality of HCT116 cells, wherein the combination treatment of 10 μM of Nutlin-3a with 10 nM of NVP-2 was the most synergistic, reaching the Bliss score of 71 (Figure 1C, bottom). In contrast, despite an induction of p53 by Nutlin-3a and a decrease in the CTD Ser2 phosphorylation by NVP-2, combinations of Nutlin-3a with NVP2 were not cytotoxic to a non-transformed colorectal epithelial cell line CCD 841 CoN (Figure S1C).

Because NVP-2 can engage CDK10 in addition to CDK9 at 1 μM dose (Olson et al., 2018), we next performed the same cytotoxicity and Bliss synergy score assays, but instead of NVP-2, we employed a selective CDK9 degrader THAL-SNS-032 and a highly selective ATP-competitive P-TEFb inhibitor iCDK9 to perturb the kinase in combination with Nutlin-3a (Lu et al., 2015; Olson et al., 2018). Confirming the results obtained with NVP-2, high doses of Nutlin-3a elicited synthetic lethality with low doses of THAL-SNS-032 and iCDK9 in a synergistic manner, reaching the highest Bliss scores of 41 and 38, respectively (Figures 1D and S1D). Likewise, increasing doses of 5-FU augmented sensitivity of HCT116 cells to sub-lethal doses of NVP-2, wherein the combination treatment of 50 μM of 5-FU with 10 nM of NVP-2 resulted in the highest Bliss score of 42 (Figure 1E).

To provide complementary evidence for the synthetic lethality triggered by PAPI, we conducted luminescence-based viability assays in which the number of metabolically active cells is determined by quantifying the levels of ATP via luciferase reaction. Here, we performed combinatorial titrations of Nutlin-3a and 5-FU with NVP-2, and calculated Bliss synergy scores for all of the combinations. Corroborating the cytotoxicity results, both p53-activating compounds synergized with the sub-lethal doses of NVP-2 to decrease viability of HCT116 cells, reaching the Bliss scores of 49 and 42 with the combination treatments of 10 μM of Nutlin-3a with 25 nm of NVP-2 and 50 μM of 5-FU with 10 nM of NVP-2, respectively (Figures S1E and S1F).

Finally, we asked whether specific pharmacological targeting of other major tCDKs can also induce synthetic lethality in combination with Nutlin-3a. We targeted CDK7, CDK8, CDK11 and CDK12/13 using YKL-5-124 (Olson et al., 2019), Senexin A (Porter et al., 2012), OTS964 (Lin et al., 2019) and THZ531 (Zhang et al., 2016) inhibitors, respectively, and conducted the combinatorial cytotoxicity and Bliss synergy score assays. While targeting CDK8 was not cytotoxic to HCT116 cells, inhibitors of other tCDKs showed modest cytotoxicity in the absence of Nutlin-3a. Importantly, Nutlin-3a treatment elicited robust synthetic lethality only with the inhibitor of CDK7, reaching the highest Bliss score of 44 (Figures S1G-S1J), which is consistent with a previous report (Kalan et al., 2017). Together, these findings establish that p53 activating compounds Nutlin-3a and 5-FU synergize strongly with nanomolar doses of highly selective antagonists of P-TEFb in eliciting cytotoxicity of HCT116 cells.

p53 is required for synthetic lethality of MDM2 inhibitor Nutlin-3a and antimetabolites with P-TEFb inhibitors

Because both Nutlin-3a and 5-FU impact cellular fate via p53, we next evaluated whether the observed synthetic lethality of PAPI depends on p53. To this end, we utilized the parental HCT116 cell line and its isogenic *TP53*$^{-/-}$ derivative, in which *TP53* was inactivated by disrupting exon 2 of both alleles using recombinant adeno-associated virus (rAAV) vector methodology (Sur et al., 2009). We exposed these lines to combinatorial titrations of Nutlin-3a and 5-FU with NVP-2 and compared their cytotoxicity and viability profiles. While the lack of p53 lowered cellular sensitivity to increasing doses of all three compounds administrated alone, it markedly blunted synthetic lethality of both p53 activators with NVP-2 (Figures 2A-2D and S2A-S2D). Specifically, cytotoxicity of the highly synergistic combinations of Nutlin-3a and 5-FU with NVP-2 dropped in *TP53* null HCT116 cells by 5.7-fold and 7.1-fold, respectively, exemplifying the pivotal contribution of p53 to the synthetic-lethal phenotype (Figure 2E).

Because 5-FU exerts its anticancer effects in part through incorporation of its metabolites into RNA and DNA (Longley et al., 2003), we next asked whether its synthetic lethality with P-TEFb inhibition depends on RNA or DNA metabolism. To address this question, we utilized ribose and deoxyribose derivatives of 5-FU, 5-fluorouridine (5-FUR) or 5-fluorodeoxyuridine (5-FdUR), respectively. Of note, 5-FdUR, also called Floxuridine, appeared among the top antimetabolites in our oncology library screen (Figures 1B and S1B) and is used to treat cancer of gastrointestinal tract that has metastasized to the liver. We therefore conducted cytotoxicity assays using the parental and *TP53* null HCT116 cells with combinatorial treatments of 5-FUR and 5-FdUR with NVP-2. We found that toxicity of both 5-FU derivatives was augmented in the presence of NVP-2 in p53-dependent fashion (Figure 2F), albeit its levels were lower in comparison to 5-FU (Figures 2E and 2F). These findings suggest that 5-FU exerts its synthetic lethality with P-TEFb antagonists through RNA and DNA metabolism. Together, we conclude that p53 enables the synthetic lethality of Nutlin-3a and antimetabolites with P-TEFb antagonists, suggesting that cells become markedly dependent on CDK9-driven transcriptional program upon activation of the p53 transcriptional program.

p53-dependent activation of apoptosis drives synthetic lethality of p53 activation and P-TEFb perturbation

Based on the evidence gathered thus far, we hypothesized that following non-genotoxic and genotoxic stabilization of p53, perturbation of P-TEFb induces cell death by apoptosis. Therefore, when combined with Nutlin-3a, targeting P-TEFb should convert cell fate choice from cell-cycle arrest to apoptosis, whereas augment apoptosis of cells exposed to sub-lethal doses of 5-FU. To address these predictions, we treated the parental and *TP53* null HCT116 cells with increasing doses of Nutlin-3a and 5-FU in the absence or presence of 10 nM of NVP-2, and conducted immunoblotting analyses to monitor induction of apoptosis and p53 pathway by determining levels of cleaved poly(ADP-ribose) polymerase (cPARP) and p53 along its direct transcriptional target, the CDK inhibitor p21, respectively. Indeed, while Nutlin-3a treatment of the parental HCT116 cells led to stabilization of p53 and induction of p21 in dose-dependent manner, robust cleavage of PARP occurred exclusively in the presence of NVP-2 (Figure 3A, left). Similarly, the sub-lethal doses of 5-FU resulted in activation of the p53 pathway but augmented cPARP levels only in combination with NVP-2 (Figure 3B, left). Importantly, none of these occurred in *TP53* null HCT116 cells (Figures 3A and 3B, right), once again underscoring the pivotal role of p53 in exerting synthetic lethality of PAPI. Confirming these findings, we observed the same apoptotic phenotype in HCT116 cells treated with Nutlin-3a and 5-FU in combination with selective CDK9 degrader THAL-SNS-032 and P-TEFb inhibitor iCDK9 (Figures 3C, 3D and S3A).

To provide additional evidence of apoptosis activation and to follow its kinetics, we performed a luminescence-based quantitative assay that measures apoptosis-induced exposure of

phosphatidylserine on the outer surface of cell membrane through time with two Annexin V fusion proteins containing fragments of NanoBit Luciferase, of which complementation is achieved through binding of Annexin V with phosphatidylserine (Dixon et al., 2016). Compared to low levels of apoptosis elicited by Nutlin-3a and NVP-2 alone, we detected robust and p53-dependent apoptosis of cells exposed to the combination, starting to be apparent at about twelve hours of the treatment (Figure 3E), which validated and extended our immunoblotting analyses above.

Finally, we asked whether only one functional *TP53* allele suffices to support activation of apoptotic cell death following concurrent p53 activation and P-TEFb inhibition. To this end, we performed the immunoblotting and kinetic apoptosis measurements by employing two additional isogenic HCT116 cell line derivatives constructed with the rAAV vector methodology. While the HCT116 *TP53*$^{R248W/+}$ cell line contains WT and transcriptionally-deficient *TP53* allele harboring R248W mutation found commonly in human cancers, the HCT116 *TP53*$^{R248W/-}$ cell line lacks functional p53 as it encodes the mutant R248W as well as the inactivated *TP53* allele (Sur et al., 2009). We treated both cell lines with increasing doses of Nutlin-3a in the absence or presence of 10 nM of NVP-2 and monitored the levels of cPARP, p53 and p21 by immunoblotting. As expected, Nutlin-3a treatment stabilized p53 in both cell lines, while p21 was induced only in HCT116 *TP53*$^{R248/+}$ cell line, underscoring the transcriptional competence of p53 encoded by the WT allele (Figure S3B). Critically, Nutlin-3a sensitized HCT116 *TP53*$^{R248W/+}$ but not HCT116 *TP53*$^{R248W/-}$ cells to NVP-2-induced apoptosis as documented by increased cleavage of PARP (Figure S3B). Corroborating these findings, kinetic analyses showed robust activation of apoptosis by the combination of Nutlin-3a and NVP-2 over the single-agent treatments only in HCT116 *TP53*$^{R248W/+}$ cells (Figure 3F). Of note, the magnitude of apoptosis induced by the combination treatment was approximately two-fold lower compared to the one observed in parental HCT116 cells, whereas the kinetic profiles in both cell lines were very similar (Figures 3E and 3F). Together, p53-dependent apoptosis drives synthetic lethality of PAPI, whereby a single WT *TP53* allele is necessary for the effect.

Sub-lethal inhibition of P-TEFb does not block transcription of key pro-apoptotic genes of the intrinsic apoptosis pathway

Upon activation, the DNA-binding transcription factor p53 elicits diverse anti-proliferative transcriptional programs, amongst which cell-cycle arrest and apoptosis are best understood (Kastenhuber and Lowe, 2017). Given the striking ability of P-TEFb antagonists to switch the fate of Nutlin-3a-treated HCT116 cells from undergoing cell-cycle arrest to apoptosis, we next set out to decipher a molecular basis for this synthetic lethality. We reasoned that alterations in transcription could explain the exquisite dependency on P-TEFb following activation of p53. Therefore, we conducted RNA sequencing analysis (RNA-seq) of poly-A enriched pools of RNA isolated from HCT116 cells treated with DMSO, 10 μM Nutlin-3a and 20 nM NVP-2 in isolation and in combination for eight hours, which precedes the onset of apoptosis triggered by the combination treatment (Figure 3E). Based on the reproducible RNA-seq data (Figure S4A), we determined differentially expressed genes (p-adj ≤ 0.001; Log2 fold-change ≥ 1).

We first analyzed transcriptional changes brought about by Nutlin-3a and examined how selective inhibition of P-TEFb with the sub-lethal 20 nM dose of NVP-2 affected these changes. As expected, Nutlin-3a elicited a highly specific transcriptional program. In comparison to DMSO treatment, expression of only 1.08% of protein-coding genes was altered (n = 10,718), amongst which 112 genes were induced, while four were repressed (Figure 4A). Using the hallmark gene set collection of the Molecular Signatures Database (MSigDB) (Liberzon et al., 2015; Subramanian et al., 2005), gene set enrichment analysis (GSEA) revealed that the p53 Hallmark Pathway was the top upregulated gene set within the Nutlin-3a-regulated program (Figure S4B), corroborating the selective targeting of the p53-MDM2 interface by Nutlin-3a. Importantly, the addition of NVP-2 to Nutlin-3a-treated cells significantly impacted expression of the Nutlin-3a-regulated genes (Figure 4B).

Because transcriptional activation by p53 is critical for triggering apoptosis (Andrysik et al., 2017), we next focused on the 112 set of genes induced by Nutlin-3a and quantified the impact of P-TEFb inhibition on this set of p53 targets. To this end, we calculated log2 fold-changes in expression for these genes in cells exposed to the Nutlin-3a and NVP-2 co-treatment compared to Nutlin-3a treatment only and created a heatmap with genes rank-ordered by decreasing changes in expression (Figure 4C). This analysis revealed that expression of twelve Nutlin-3a-induced genes increased further upon the addition of NVP-2, while expression of the remaining 100 genes either did not increase as much as with NVP-2 treatment alone (35 genes with log2 fold-change ≥ 1 compared to DMSO, 77 with log2 fold-change > 0) or decreased in expression compared to pre-Nutlin-3a levels (33 with log2 fold-change < 0 compared to DMSO). We next divided these 100 genes into four bins based on the magnitude of repression by NVP-2. Given our evidence that Nutlin-3a synergizes with sub-lethal doses of NVP-2 to induce cell death by apoptosis, we reasoned that genes critical to the onset of apoptosis should not be exceedingly repressed by NVP-2. Indeed, we identified pro-apoptotic genes of the intrinsic apoptosis pathway, including *AEN*, *BAX*, *BBC3* and *ATF3*, amongst genes showing no or little repression by NVP-2 (BIN 1), while another member of this pathway, *APAF1*, was repressed only moderately (BIN 2).

In metazoans, apoptosis can be initiated via two distinct pathways: the mitochondria-mediated intrinsic pathway and the death receptor-mediated extrinsic pathway. Among the pro-apoptotic genes which we identified as to a large degree resistant to sub-lethal inhibition of P-TEFb, *BAX*, *BBC3*, and *APAF1* code for BCL-2-associated X protein (BAX), p53-upregulated modulator of apoptosis (PUMA) and apoptotic protease-activating factor 1 (APAF1), respectively, which are critical regulators of the intrinsic pathway (Singh et al., 2019). Namely, the balance between pro-apoptotic and pro-survival members of the BCL-2 family of proteins governs mitochondrial outer membrane permeabilization (MOMP), which is the critical step at which a cell irreversibly commits to undergoing apoptotic cell death (Tait and Green, 2013). Specifically, pro-apoptotic members, such as BCL-2-interacting mediator of cell death (BIM), truncated BH3-interacting domain death agonist (tBID) and PUMA, can be bound and sequestered by pro-survival members such as BCL-2, B cell lymphoma extra large (BCL-X_L) or myeloid cell leukaemia 1 (MCL1) (Kale et al., 2018). However, when these pro-survival proteins are saturated or absent, the balance is tipped in favor of the pro-apoptotic members that can engage and activate either or both of the pro-apoptotic BAX and/or BCL-2 antagonist/killer (BAK), of which pore-forming oligomers cause MOMP, resulting in the release of apoptogenic molecules such as cytochrome *c* from the mitochondrial intermembrane space. In turn, cytochrome *c* binds APAF1 in the cytosol to assemble the heptameric apoptosome (Dorstyn et al., 2018), which serves as a platform for the autocleavage of the initiator procaspase 9 that subsequently leaves the complex to activate the downstream effector caspases 3 and 7, culminating in dismantling of the cell.

Therefore, we next independently assessed our RNA-seq findings by conducting RT-qPCR analysis to determine mRNA levels of *BAX*, *BBC3*, and *APAF1.* Because 10 μM of Nutlin-3a exhibited the highest synergy in eliciting synthetic lethality with 10 nM of NVP-2 (Figure 1C), we exposed HCT116 cells to these treatments individually and in combination. Supporting the RNA-seq data, we observed that Nutlin-3a-induced expression of *BAX* was decreased only moderately by NVP-2, while that of *BBC3* and *APAF1* was elevated even further (Figure 4D). Together, these findings show that inhibiting P-TEFb with sub-lethal doses of NVP-2 leaves transcription of p53-dependent genes critical for executing the intrinsic apoptosis pathway largely unhindered.

Transcriptional induction of pro-apoptotic genes enables synthetic lethality of p53 activation and P-TEFb inhibition via the intrinsic apoptosis pathway

The above gene expression findings raised an inviting possibility that the synthetic lethality of PAPI could be driven at least in part by activation of the intrinsic apoptosis pathway. Furthermore, we postulated that an efficient blockade of Pol II transcription should attenuate synthetic lethality of the combination treatment via diminishing the transcriptional induction of p53 target genes. To monitor execution of the intrinsic apoptosis pathway, we utilized a luminescence-based quantitative

assay that measures cleavage of a pro-luminogenic substrate by caspase 9. Using HCT116 cells, we observed that 10 μM of Nutlin-3a and 10 nM of NVP-2 treatment alone did not stimulate caspase 9 activity above the levels of DMSO control. In contrast, the combination treatment led to synergistic activation of caspase 9 (Figure 4E). As postulated, this activation was blunted by the addition of 500 nM of NVP-2 and Pol II transcription inhibitor triptolide, which acts by inhibiting the ATPase activity of the TFIIH subunit XPB (Titov et al., 2011). Importantly, we monitored mRNA levels of the key intrinsic apoptosis genes *BAX*, *BBC3*, and *APAF1* under the same treatments using RT-qPCR. Consistent with the caspase 9 activation findings, both Pol II inhibitors ablated the Nutlin-3a-induced expression of *BAX*, *BBC3*, and *APAF1*, particularly within the combination treatment (Figures 4F and S4C).

To gather complementary evidence on the requirement of Pol II transcription for the synthetic lethal phenotype, we exposed HCT116 cells again to 10 μM of Nutlin-3a and 10 nM of NVP-2 alone and together in the absence or presence of triptolide and monitored the levels of CDK9, cPARP, p53 and p21 by immunoblotting. While the addition of triptolide augmented stabilization of p53 across all conditions, it abrogated PARP cleavage and induction of p21 (Figure 4G), confirming that blocking Pol II transcription is incompatible with apoptosis triggered by the combination treatment. Likewise, triptolide blunted synthetic lethality of HCT116 cells exposed to the combinatorial titrations of Nutlin-3a with NVP-2 as demonstrated by cytotoxicity assays (Figure S4D). These findings are consistent with our initial observation that increasing the dose of P-TEFb antagonists NVP-2, THAL-SNS-032 and iCDK9 beyond the one eliciting a maximal cytotoxicity precluded cell death when administered alone and in combination with Nutlin-3a or 5-FU in a progressive manner (Figures 1 and 2). Corroborating this notion, the levels of cPARP and the p53 target p21 peaked at 50 nM of NVP-2 and 500 nM of iCDK9, while higher doses of both inhibitors, namely, 250 nM or 500 nM of NVP-2 and 2.5 μM of iCDK9, diminished apoptosis and p53-driven transcription as evidenced by attenuated cleavage of PARP and induction of p21 (Figures S4E and S4F). Together, execution of the intrinsic apoptosis pathway drives the synthetic lethality of PAPI, and transcriptional induction of key pro-apoptotic genes is a pre-requisite for cell death by apoptosis.

Inhibition of P-TEFb hampers oncogenic PI3K-AKT pathway via transcriptional repression of genes encoding key components of PI3K signaling

Our gene expression and functional findings show that sub-lethal doses of NVP-2 do not impede the pro-apoptotic transcriptional program governed by p53. However, it remained unclear why do cells become markedly dependent on CDK9-driven transcription upon activation of p53. To address this critical question, we next focused on transcriptional changes elicited by NVP-2. Compared to Nutlin-3a, NVP-2 treatment had a much broader impact on gene expression, underscoring a pivotal role of P-TEFb in transcription by Pol II. Applying our criteria, we identified 22.69% DE protein-coding genes (n = 10,728), amongst which 2137 genes were repressed, while 297 were induced (Figure 5A). These widespread alterations in transcription very likely affect a variety of processes, many of which might promote apoptosis of HCT116 cells treated by Nutlin-3a. Nevertheless, we suspected that NVP-2 treatment might impact a key oncogenic pathway, enabling synthetic lethality of the combination treatment.

Amongst the set of genes repressed by NVP-2, we were very intrigued to find genes encoding key components of the oncogenic phosphoinositide 3-kinase (PI3K)–AKT signaling pathway, including class IA PI3K catalytic subunits p110α (*PIK3CA*) and p110β (*PIK3CB*), their regulatory subunit p85α (*PIK3R1*), class II PI3K catalytic subunit C2β (*PIK3C2B*), class III PI3K regulatory subunit p150 (*PIK3R4*), and a receptor tyrosine kinase (RTK) adaptor protein IRS-2 (*IRS2*) (Figure 5B). PI3K-AKT is the most commonly deregulated pathway in human cancers (Fruman et al., 2017). Analyses across cancer lineages identified *PIK3CA a*s the most frequently mutated single oncogene (Lawrence et al., 2014), of which the H1047R hotspot mutation within the kinase domain of p110α, also present in HCT116 cells, promotes localization of the mutant kinase to plasma membrane

(Mandelker et al., 2009). Hence, the activating mutation circumvents the activation route of WT PI3K, wherein ligand-induced activation of RTK and subsequent tyrosine phosphorylation of its cytosolic domain or adaptor protein paralogues IRS1/2 creates phospho-tyrosyl binding sites for SH2 domains of the PI3K regulatory subunit, which allosterically activates and recruits the PI3K heterodimer to the plasma membrane. In turn, PI3K phosphorylates phosphatidylinositol 4,5-bisphosphate (PtdIns(4,5)P_2) to produce the second messenger phosphatidylinositol 3,4,5-trisphosphate (PtdIns(3,4,5)P_3), leading to the recruitment and full activation of the serine/threonine protein kinase AKT, promoting cell survival, growth and proliferation (Figure 5B).

We hypothesized that selective inhibition of P-TEFb interferes with the signaling through the PI3K-AKT pathway at the level of target gene transcription, thus contributing to converting the fate of Nutlin-3a-treated HCT116 cells from undergoing cell-cycle arrest to apoptosis. We first conducted RT-qPCR analysis using HCT116 cells treated with increasing doses of NVP-2 to assess mRNA levels of *PIK3CA*, *PIK3CB*, *PIK3R1*, *PIK3C2B*, *PIK3R4* and *IRS2*, and found that their levels decreased in a dose-dependent manner while mRNA levels of *ACTB* remained largely unaffected, which validated the RNA-seq findings (Figure 5C). To provide further evidence that transcription of the PI3K-related genes depends on P-TEFb, we next employed quantitative chromatin immunoprecipitation (ChIP-qPCR) assays to monitor the occupancy of total Pol II as well as its CTD Ser2 and Ser5 phosphorylated forms at the transcription start site (TSS) and within gene body (GB) of three PI3K genes critical for the signaling through class IA PI3K using control and NVP-2-treated HCT116 cells. Namely, while CDK7 regulates Pol II transcription by phosphorylating Ser5 and Ser7 residues of the CTD (Parua and Fisher, 2020), P-TEFb does so by targeting Ser2 residues (Core and Adelman, 2019; Zhou et al., 2012). To account for the changes in Pol II occupancy at the genes elicited by NVP-2, we normalized signals of the Ser2 and Ser5 phosphorylated forms to those of total Pol II. This analysis showed that unlike in the case of the Ser5 levels, a sub-lethal dose of NVP-2 resulted in significant drop of the Ser2 levels at most tested locations of *PIK3CA*, *PIK3R1* and *IRS2* (Figure 5D), confirming that NVP-2 decreases transcription of this set of PI3K-AKTpathway genes by specifically targeting P-TEFb.

Based on these results, we reasoned that inhibition of P-TEFb should decrease protein levels of class IA PI3K heterodimers and adaptor protein IRS-2, leading to lowered activity of the PI3K-AKT signaling. Because mTORC2 promotes maximal activity of AKT by phosphorylating Ser473 (Ser473-P AKT) within its hydrophobic motif (Fruman et al., 2017), we used phospho-specific antibody recognizing this AKT modification as a readout of class IA PI3K activation. Indeed, using immunoblotting analysis, we found that NVP-2 treatment decreased protein levels of p110α, p110β, p85α, and IRS-2 in a dose-dependent fashion (Figure 5E). Critically, these effects were accompanied by gradual attenuation of the PI3K signaling as determined by decreasing Ser473-P AKT levels, while total levels of AKT were affected minimally. In contrast, activity of the mitogen-activated protein kinase signaling pathway which we monitored using phospho-specific and total ERK1/2 antibodies did not change, highlighting specificity of P-TEFb for the PI3K-AKT pathway. Together, we conclude that inhibition of P-TEFb hampers the oncogenic PI3K-AKT signaling cascade by repressing transcription of genes encoding key components of this pathway.

Pharmacological targeting of PI3K-AKT pathway elicits synthetic lethality with activators of p53

Our evidence gathered thus far supports a model whereby decreased activity of the pro-survival PI3K-AKT pathway is a driver of heightened dependency on CDK9-driven transcription upon activation of p53. Hence, we hypothesized that direct pharmacological targeting of PI3K-AKT pathway elicits synthetic lethality with non-genotoxic and genotoxic activators of p53. To address this prediction, we conducted cytotoxicity assays using the parental and *TP53* null HCT116 cells which we treated with Nutlin-3a, 5-FU, and a potent and selective inhibitor of class I PI3K Pictilisib (GDC-0941) alone or in combination (Folkes et al., 2008). While all compounds provoked limited toxicity over the DMSO control when administered alone, Pictilisib treatment elicited synthetic

lethality with both activators of p53 in a synergistic manner in parental but not *TP53* null cells, reaching the Bliss scores of 41 and 38 with Nutlin-3a and 5-FU, respectively (Figure 5F).

To extend these findings, we next tested whether attenuating PI3K-AKT pathway triggers p53-dependent apoptosis of HCT116 cells treated with Nutlin-3a. We exposed the parental and *TP53* null HCT116 cells to increasing doses of Nutlin-3a in the absence or presence of Pictilisib and performed immunoblotting analyses to monitor apoptosis as well as activity of p53 and PI3K-AKT pathways by determining levels of cPARP, p53, p21 as well as total and Ser473-P AKT. Indeed, while Nutlin-3a treatment of the parental HCT116 cells led to stabilization of p53 and induction of p21 in dose-dependent fashion in the absence or presence of Pictilisib, cPARP levels increased only upon blocking PI3K-AKT pathway (Figure 5G, left). We observed none of these in *TP53* null HCT116 cells (Figure 5G, right), highlighting again the requirement of p53 for synthetic lethality of p53 activation and PI3K-AKT inhibition. Together, these results demonstrate that inhibiting class I PI3K also switches the fate of Nutlin-3a-treated cells from cell-cycle arrest to apoptosis. Furthermore, they suggest that compromising the PI3K-AKT pathway through transcriptional repression of genes encoding key components of the pathway contributes to the synthetic lethality of PAPI.

Synthetic lethality of p53 activation and P-TEFb inhibition remains effectual in three-dimensional spheroid culture system

Three-dimensional (3D) spheroid cell cultures are a widely used platform for pre-clinical assessment of anti-cancer treatments (Zanoni et al., 2016). In contrast to monolayer cultures, spheroids possess several *in vivo* characteristics of tumor microenvironments, including well-organized spatial architecture of cells with different proliferation status, complex cell-cell contacts, oxygen and nutrient gradients and rewired metabolism. Moreover, they better model drug penetration, response and resistance. Therefore, we assessed whether the synthetic lethal combination treatments defined in this study remained effectual in 3D cell culture setting.

For these experiments, we cultured HCT116 cells in low-attachment, U-shaped plates for forty-eight hours to establish scaffold-free spheroids of about 400 μm in size. We then tested efficacy of the synthetically lethal combination of PAPI by treating the spheroids for three days with the DMSO control, Nutlin-3a, 5-FU and NVP-2 alone or in combination as indicated (Figure 6A). To assess the viability of spheroids, we used confocal microscopy to image spheroids stained with a cocktail of three dyes. We identified live cells with an intracellular esterase activity indicator Calcein AM emitting green fluorescence, dead cells with a cell membrane impermeable DNA stain DRAQ7 emitting red fluorescence, and total cell nuclei with the cell membrane permeable DNA stain Hoechst emitting blue fluorescence. When administered alone, all compounds had a modest impact on spheroids. While both 5-FU and NVP-2 treatment resulted in limited toxicity, Nutlin-3a yielded considerably smaller spheroids, indicative of p53-dependent cell-cycle arrest. Critically, both activators of p53 sensitized the spheroids to the sub-lethal dose of NVP-2 as evidenced by massive cell death in the combination treatments that was accompanied by an obvious disfiguration of the spheroid architecture (Figures 6A and S5A). To quantify viability of spheroids, we determined a ratio between dead and live cells for each spheroid by dividing intensities of Calcein AM and DRAQ7 staining in segmented cells, which we further normalized to the total spheroid cell number determined by Hoechst staining. Corroborating the confocal images, Nutlin-3a and 5-FU synergized with NVP-2 in eliciting death of spheroids (Figure 6B).

Finally, we conducted quantitative kinetic measurements to monitor apoptosis of spheroids exposed to all combination treatments which we defined in this study as synthetic lethal using monolayer cultures. We detected negligible levels of apoptosis when analyzing HCT116 spheroids treated for three days with Nutlin-3a, 5-FU, NVP-2, and Pictilisib. In contrast, the respective combination treatments elicited robust apoptosis in a highly synergistic manner (Figures 6C-6E, left). As anticipated, p53 was required for synthetic lethality because the combinations failed to result in

apoptosis of *TP53* null HCT116 spheroids (Figures 6C-6E, right). Further underscoring the critical role of p53, Nutlin-3a treatment sensitized HCT116 *TP53*$^{R248/+}$ but not p53-deficient HCT116 *TP53*$^{R248/-}$ spheroids to NVP-2-induced apoptosis (Figure S5B). In addition, both 5-FUR and 5-FdUR, the ribose and deoxyribose derivatives of 5-FU, elicited apoptosis in the presence of NVP-2 (Figures S5C and S5D). Finally, within the canonical PAPI combination treatment, we replaced P-TEFb inhibitor NVP-2 with DT-061, a prototypical small-molecule activator of PP2A that stabilizes and allosterically activates a specific heterotrimeric PP2A holoenzyme to antagonize phosphorylation of key P-TEFb substrates including SPT5 and the CTD of Pol II (Leonard et al., 2020; Vervoort et al., 2021). Therefore, we postulated that PP2A activation should akin to P-TEFb inhibition synergize with p53 activation in inducing apoptotic cell death. Indeed, non-genotoxic and genotoxic activation of p53 by Nutlin-3a and 5-FU, respectively, sensitized HCT116 spheroids to apoptosis by PP2A activator DT-061 (Figures S5E and S5F), illustrating possibilities to expand further the arsenal of synthetic lethal combinations of PAPI. Together, we conclude that the synthetic lethal combination treatments uncovered with monolayer cell cultures remained effectual in the translational spheroid setting.

DISCUSSION

The central role of tCDKs in gene control and their emergence as a vital player in increasing number of cancer types has elevated the interest in these kinases as potential therapeutic targets. In this study, we harnessed a comprehensive oncology library to identify compounds that rendered colon cancer-derived cells dependent on transcription driven by P-TEFb. By focusing on antimetabolites and MDM2 inhibitors, the broadly used chemotherapeutics and small-molecule PPI inhibitors with a huge clinical potential, respectively, we took a multidisciplinary approach to reveal a set of combination treatments within the PAPI framework that triggered cell death by apoptosis in synergistic and p53-dependent fashion as well as underlying molecular events driving the synthetic lethality. Finally, combination treatments elicited apoptosis to dismantle cancer cell spheroid cultures, providing impetus for assessing effectiveness of the treatments in translational settings in the future.

Mechanistically, we investigated a molecular basis that governs the ability of P-TEFb inhibitor NVP-2 to switch the fate of cells harboring Nutlin-3a-induced p53 from cell-cycle arrest to apoptosis. Our evidence shows that the fate switching can be explained by differential sensitivity of key sets of genes to P-TEFb inhibition. Specifically, we find that sub-lethal doses of NVP-2 fail to block p53-induced transcription of key genes that enable execution of the intrinsic apoptosis pathway, which includes *BAX*, *BBC3*, and *APAF1*. Concomitantly, these NVP-2 doses repress pro-survival genes encoding key components of the PI3K-AKT signaling pathway, including *PIK3CA*, *PIK3CB*, *PIK3R1*, *PIK3C2B*, *PIK3R4* and *IRS2,* which culminates in decreased levels of their protein counterparts and compromised activity of this critical oncogenic pathway, contributing to the synthetic lethality of the combination treatment. We provide two main lines of evidence in support of the notion that this dichotomous response to P-TEFb inhibition is a key driver of p53-dependent apoptosis. First, shutdown of Pol II transcription with triptolide or high dose of NVP-2 does not only attenuate the induction of pro-apoptotic genes by p53, but also blocks the onset of apoptosis despite stabilizing p53 under these conditions. Second, pharmacological attenuation of the PI3K-AKT pathway with the class I PI3K inhibitor Pictilisib phenocopies the ability of sub-lethal P-TEFb inhibition to switch the cell fate. Together, we define a framework of transcriptional alterations by highly selective small-molecule inhibitors that seal the fate of cancer cells in an irreversible manner. Further mechanistic studies are needed to decipher why is transcription of the critical apoptotic genes insensitive to sub-lethal inhibition of P-TEFb and what series of events govern execution of the intrinsic apoptosis pathway under the altered transcriptional landscape.

Our work contributes to the growing repertoire of synthetic lethal interactions with inhibitors of P-TEFb. Previous studies identified genetic and epigenetic alterations in cancer cells which heightened the reliance on P-TEFb. The prime examples are amplification of *MYC* in a variety of cancers including colorectal cancer, and rearrangement of *MLL1* in hematological malignancies, wherein both oncoproteins relocate P-TEFb to their key loci to drive oncogene-specific transcription programs, providing an explanation for increased sensitivity to P-TEFb inhibitors (Vervoort et al., 2022). In addition, perturbation of several targets, including BRD4 (Lu et al., 2015; Moreno et al., 2017), PARP (Li et al., 2020), CDK2 (Poon et al., 2020), and MDM2 (Štětková et al., 2020), was reported to elicit lethality of cancer cells in combination with inhibitors of P-TEFb. However, many of these studies employed P-TEFb inhibitors exhibiting sub-optimal selectivity, which suggested that targeting of additional kinases contributed to the lethality. By conducting oncology library screen with the highly selective inhibitor NVP-2, we here validate most of the previous reports and identify novel synthetic lethal interactions requiring further investigation. Importantly, on the basis of our mechanistic studies, we reveal that inhibiting class I PI3K and activating PP2A also sensitizes cancer cells to Nutlin-3a and 5-FU. As PI3K and PP2A represent important targets in cancer (Fruman et al., 2017; Vainonen Julia et al., 2021), our work therefore offers new avenues for rational design of combination therapies with p53-activating compounds.

Finally, our study provides a rationale for improving chemotherapeutic interventions with highly selective targeting of P-TEFb. Importantly, it promises to reinvigorate the prospects of reactivation of tumor suppressive capabilities of p53 in cancer with Nutlin-3a-based small molecules. Since the discovery of Nutlin-3a nearly twenty years ago, there has been a tremendous interest in delivering this class of non-genotoxic activator of p53 into the clinic (Konopleva et al., 2020). While up to 50% of cancers carry loss-of-function *TP53* mutations in both alleles of the gene, the remaining 50% keep p53 in check through other means such as *MDM2* amplification, making WT p53 an appealing target for therapeutic intervention. However, reactivating p53 with Nutlin-3a and its derivatives triggers apoptosis only in a small fraction of cancer cell types and elicits instead a reversible and thus therapeutically undesirable cell-cycle arrest in most cell lines examined (Tovar et al., 2006). Therefore, our demonstration that selective antagonists of P-TEFb switch the fate of Nutlin-3a-treated monolayer and spheroid cell cultures from reversible cell-cycle arrest to irreversible apoptotic cell death could come to the rescue. Furthermore, we find that inhibiting class I PI3K and activating of PP2A also leads to the cell fate switching phenotype. Thus, our work contributes additional avenues to the ongoing efforts of developing combinatorial treatments with non-genotoxic p53 activators (Konopleva et al., 2020). Because small-molecule MDM2 degraders are presumed to exhibit increased potency and therapeutic index over MDM2 inhibitors (Li et al., 2019), combining the degraders with highly selective P-TEFb and PI3K antagonist or PP2A agonists shall be further investigated.

EXPERIMENTAL PROCEDURES

Cell culture

HCT116 parental cell line and its derivatives were cultured in McCoy's medium supplemented with 10% FBS and antibiotics.

Chemicals

Senexin A, OTS964, Pictilisib, Nutlin-3a, 5-fluorouracil, and Triptolide were from Selleckchem. 5-Fluorouridine (FUR), Floxuridine (5-FUdR) were from MCE Chemicals. THZ531, YLK-5-124, NVP-2, and SNS032-THAL inhibitors were received from Nathaniel Gray's Lab, Dana Farber Institute (Boston, USA), i-CDK9 was a gift from Qiang Zhou's Laboratory (UC Berkley, USA). PP2A activator DT-061 was a gift from Jukka Westermarck's Laboratory (University of Turku, Finland).

Drug library

FO5A version of the FIMM oncology collection was obtained from various commercial chemical vendors (Pemovska et al., 2013). The library comprised 527 single compounds and 1 drug combination, of which 28% represented approved anticancer drugs, 55% - emerging investigational compounds, and 17% - chemical probes covering a wide range of molecular targets (Figure S1A).

Drug Sensitivity and Resistance Testing

Drug Sensitivity and Resistance Testing was performed essentially as described previously (Pemovska et al., 2013) with minor modifications. CellTox Green (CTX) cytotoxicity reagent (Promega) was added to cell suspension at a final dilution 1:1000 before seeding cells on the drug plates in 25 μl final volume. After 72h of incubation with drugs, the number of dead cells was measured using CellTox Green fluorescence with a Pherastar FS multimode platereader (BMG Labtech) according to manufacturer's instructions.

Data analysis

The cell viability data were processed using an in-house developed drug screening data analysis application Breeze (Potdar et al., 2020). The data were normalized to negative control (DMSO only) and positive control wells (containing 100 μmol/L benzethonium chloride, effectively killing all cells). Drug sensitivity scores (DSS) (Yadav et al., 2014b) were calculated for each treatment. Differential DSS (dDSS) was further calculated by subtracting DSS values of NVP-2-containing plate sets from those of the control plate set. Positive dDSS values indicated that NVP-2 may enhance the cytotoxic effect of a given drug, while negative dDSS values suggest the opposite effect. The waterfall plots showing drugs having significant differences in dDSS across the screens were generated using R programming language with the help of package ggplot2.

Cytotoxicity, cell survival, and apoptosis assays

HCT116 cells were seeded on 96-well plates 16 h before the experiment to ensure 80% confluency. Cytotoxicity was evaluated using CellTox Green Cytotoxicity (CTxG) from Promega. CellTox Green Dye (McDougall and Dwight, 2010) was added to the cells simultaneously with combinations of chemicals. Fluorescence, in the case of CTxG and luminescence in the case of CTG assay, were measured using PerkinElmer Victor X3 reader according to the protocols given by the assay supplier after 48 hours of drug combination treatments. The cell viability of the cells was tested with the assistance of Cell Titer Glo 2 Assay from Promega (Crouch et al., 1993). Activation of apoptosis was assessed using Real Time-Glo Annexin V Apoptosis and Necrosis Assay (Promega). In this assay, PerkinElmer Victor X3 Reader was used to read luminescence at the indicated time points. All

experiments were performed in biological triplicates and for each replicate, at least two wells per condition were measured to obtain an average raw fluorescence or luminescence value.

Analysis of cytotoxicity and cell survival data

To obtain % of inhibition in CTxG and CTG assays the raw fluorescence and luminescence values were presented as a ratio to the DMSO-treated control, normalized to the difference between DMSO and positive control sample representing maximum cytotoxicity. Maximum cytotoxicity was defined as a maximum fluorescence value obtained from the samples with absolute cell death. An average of three biological replicates was then plotted using the Seaborn Python data visualization library (https://github.com/mwaskom/seaborn). To calculate Bliss synergy scores Synergyfinder was used and data on individual concentrations were downloaded and plotted using Seaborn.

Immunoblotting

Whole-cell extracts (WCE) were prepared by resuspension of the cell pellets in lysis buffer C (20 mM Tris-HCl, 0.5% NP-40, 150 mM NaCl, 1.5 mM MgCl2, 10 mM KCl, 10% Glycerol, 0.5 mM EDTA, pH 7.9) on ice for 1 h in the presence of EDTA-free Protease Inhibitor Cocktail (Sigma). Lysates were cleared by centrifugation and then boiled in 95oC of SDS running buffer supplied with 10% of 2-mercaptoethanol (Sigma) for 5 min, separated in 10% SDS-PAGE and transferred to nitrocellulose membranes.

RNA Extraction and RT-qPCR

80% confluent HCT116 cells grown on 6-well plates were treated with specified drug combinations or 0.1% DMSO. TRI Reagent (Sigma) was used to extract RNA from the cell pellets. The residual DNA was removed using the Turbo DNA-Free kit (Thermo Fisher Scientific). To obtain cDNAs from the extracted RNA, M-MLV reverse transcriptase (Thermo Fisher Scientific) treatment was performed using random hexamers (Thermo Fisher Scientific) according to the manufacturer's instructions. qPCR reactions were performed with diluted cDNAs using primer pairs spanning the exon-intron junction of tested genes. qPCR was performed with FastStart Universal SYBR Green QPCR Master (Rox) from Sigma using Stratagene Mx3005 qPCR machine or Roche LightCycler 480. Primers were designed using PrimerQuest Tool and obtained from Integrated DNA Technologies. Relative expression of transcripts was quantified using the MxPro QPCR Software v4.10. GAPDH mRNA values were used to normalize levels of RNA expression. At least three independent experiments were performed, and results were presented as the mean ± s.e.m.

Total RNA sequencing

For total RNAseq, the HCT116 cells were grown as described above and treated with indicated drug concentrations for 8 h, followed by total RNA extraction using the NucleoBond RNA kit in accordance with the manufacturer’s instructions. The sequencing was performed by the Functional Genomics Unit.

Analysis of RNA Sequencing data sets

RNA-seq reads were mapped against the human genome (hg38) and human rRNA sequences using ContextMap version 2.7.9 (Bonfert et al., 2015) using BWA (Li and Durbin, 2009). Number of read counts per gene and exon were determined from the mapped RNA-seq reads in a strand-specific manner using featureCounts (Liao et al., 2014) and gene annotations from Gencode version 25 (Frankish et al., 2021). Differential gene expression analysis was performed using edgeR (Robinson et al., 2010). P-values were adjusted for multiple testing using the method by Benjamini and Hochberg (Benjamini and Hochberg, 1995) and genes with an adjusted p-value ≤ 0.001 were considered significantly differentially expressed. For further analysis, we included only genes expressed (Reads per kilo base per million mapped reads (RPKM) >=1) in at least condition. Analysis workflows were implemented and run using the Watchdog workflow management system

(Kluge and Friedel, 2018). Vulcano plots, heatmaps and other figures were created in R [REF: R Core Team (2016). R: A language and environment for statistical computing. R Foundation for Statistical Computing, Vienna, Austria. URL https://www.R-project.org/.]. Hierarchical clustering analysis in heatmaps was performed using Ward's clustering criterion and Euclidian distances. Gene set enrichment analysis (GSEA) on log2 fold-changes for protein-coding genes was performed using the command line tool from http://www.gsea-msigdb.org/ (version 4.0.2) (Subramanian et al., 2005) and hallmark gene sets from Molecular Signatures Database (MSigDB). Heatmaps were created using the heatmap library in R [REF: R Core Team (2016). R: A language and environment for statistical computing. R Foundation for Statistical Computing, Vienna, Austria. URL https://www.R-project.org/.] and clustering of genes in heatmaps was performed using Ward's clustering criterion (Murtagh and Legendre, 2014) and Euclidean distances.

Drug treatment and imaging of HCT116 spheroids

The HCT116 cell were plated into 384-well, ultra low attachment, Corning U-bottom, black clear-bottom imaging plates (Corning 3830) at density of 400 cells/well in the appropriate media at 37°C and 5% CO2 and spun down at 200g for 10 minutes. After 48 hours, the spheroids were exposed to the indicated concentrations of DMSO-diluted drugs for 4 days. Following incubation with test compounds, spheroids were stained with a mixture of three PBS-diluted dyes: 1 µM calcein AM, 6 µM of DRAQ7TM (Invitrogen™ D15106) and 1x Hoechst 33342 (Invitrogen™ L3224A, D15106 and R37605, respectively. Dye solutions were prepared immediately before use and added directly to media without aspiration followed by incubation for 6 hours before imaging. Imaging was performed with a Opera Phenix confocal spinning-disk high content screening microscope (PerkinElmer, Inc., Waltham, MA, USA, High Content Imaging and Analysis Unit, FIMM, HiLIFE, University of Helsinki, Finland). Screening was conducted with a 40x water immersion objective (NA 1.1, working distance 0.62 mm, depth of focus 1.2 µm) and four excitation lasers (405 nm with emission band-pass filter 435/480; ex 488, em 500/550; ex 647, em 650/760). Fields of view were automatically selected from a pre-scan iimage with a 10% overlap using 90 predetermined Z focus planes with laser-based autofocusing. The images were captured with two Andor Zyla sCMOS cameras (16 bit, field of view 320 x 320 µm2, effective xy resolution 0.33 µm). 3D Image analysis was performed with PerkinElmer Harmony 4.9 software. Cells were segmented according to the nuclear staining with a cytoplasmic mask from combined channel images. Results were shown as a ratio of integrated intensities from Calcein AM and DRAQ7 staining in segmented cells and normalized against the observed cell number as quantified with nuclear DNA staining. The final results were presented as a fold change in cytotoxicity as compared to the DMSO control.

Quantification and statistical analysis

Differential gene expression analysis of 4sU-seq data was performed using edgeR (Robinson et al., 2010). P-values obtained from edgeR were corrected by multiple testing using the method by Benjamini and Hochberg (Benjamini and Hochberg, 1995) for adjusting the false discovery rate (FDR) and a p-value cutoff of 0.01 was applied. Data shown for all qPCR-based experiments and functional assays were collected from at least 3 biological replicates as indicated in individual figure legends and are presented as means ± s.e.m. Statistical significance and *P* values were determined by one-tailed Student's *t* test performed between the indicated paired groups of biological replicates. Where the results were not statistically significant, *P* values are not indicated.

REFERENCES

Andrysik, Z., Galbraith, M.D., Guarnieri, A.L., Zaccara, S., Sullivan, K.D., Pandey, A., MacBeth, M., Inga, A., and Espinosa, J.M. (2017). Identification of a core TP53 transcriptional program with highly distributed tumor suppressive activity. Genome research *27*, 1645-1657.

Benjamini, Y., and Hochberg, Y. (1995). Controlling the False Discovery Rate: A Practical and Powerful Approach to Multiple Testing. Journal of the Royal Statistical Society. Series B (Methodological) *57*, 289-300.

Bentley, D.L. (2014). Coupling mRNA processing with transcription in time and space. Nature Reviews Genetics *15*, 163-175.

Blazek, D., Kohoutek, J., Bartholomeeusen, K., Johansen, E., Hulinkova, P., Luo, Z., Cimermancic, P., Ule, J., and Peterlin, B.M. (2011). The Cyclin K/Cdk12 complex maintains genomic stability via regulation of expression of DNA damage response genes. Genes Dev *25*, 2158-2172.

Bonfert, T., Kirner, E., Csaba, G., Zimmer, R., and Friedel, C.C. (2015). ContextMap 2: fast and accurate context-based RNA-seq mapping. BMC Bioinformatics *16*, 122.

Boshuizen, J., and Peeper, D.S. (2020). Rational Cancer Treatment Combinations: An Urgent Clinical Need. Molecular Cell *78*, 1002-1018.

Bradner, J.E., Hnisz, D., and Young, R.A. (2017). Transcriptional Addiction in Cancer. Cell *168*, 629-643.

Bunz, F., Hwang, P.M., Torrance, C., Waldman, T., Zhang, Y., Dillehay, L., Williams, J., Lengauer, C., Kinzler, K.W., and Vogelstein, B. (1999). Disruption of p53 in human cancer cells alters the responses to therapeutic agents. The Journal of clinical investigation *104*, 263-269.

Core, L., and Adelman, K. (2019). Promoter-proximal pausing of RNA polymerase II: a nexus of gene regulation. Genes Dev *33*, 960-982.

Cossa, G., Parua, P.K., Eilers, M., and Fisher, R.P. (2021). Protein phosphatases in the RNAPII transcription cycle: erasers, sculptors, gatekeepers, and potential drug targets. Genes Dev *35*, 658-676.

Dixon, A.S., Schwinn, M.K., Hall, M.P., Zimmerman, K., Otto, P., Lubben, T.H., Butler, B.L., Binkowski, B.F., Machleidt, T., Kirkland, T.A.*, et al.* (2016). NanoLuc Complementation Reporter Optimized for Accurate Measurement of Protein Interactions in Cells. ACS Chem Biol *11*, 400-408.

Dorstyn, L., Akey, C.W., and Kumar, S. (2018). New insights into apoptosome structure and function. Cell Death & Differentiation *25*, 1194-1208.

Eick, D., and Geyer, M. (2013). The RNA Polymerase II Carboxy-Terminal Domain (CTD) Code. Chemical Reviews *113*, 8456-8490.

Folkes, A.J., Ahmadi, K., Alderton, W.K., Alix, S., Baker, S.J., Box, G., Chuckowree, I.S., Clarke, P.A., Depledge, P., Eccles, S.A.*, et al.* (2008). The identification of 2-(1H-indazol-4-yl)-6-(4-methanesulfonyl-piperazin-1-ylmethyl)-4-morpholin-4-yl-thieno[3,2-d]pyrimidine (GDC-0941) as a potent, selective, orally bioavailable inhibitor of class I PI3 kinase for the treatment of cancer. Journal of medicinal chemistry *51*, 5522-5532.

Frankish, A., Diekhans, M., Jungreis, I., Lagarde, J., Loveland, J.E., Mudge, J.M., Sisu, C., Wright, J.C., Armstrong, J., Barnes, I.*, et al.* (2021). GENCODE 2021. Nucleic Acids Res *49*, D916-d923.

Fruman, D.A., Chiu, H., Hopkins, B.D., Bagrodia, S., Cantley, L.C., and Abraham, R.T. (2017). The PI3K Pathway in Human Disease. Cell *170*, 605-635.

Gajdušková, P., Ruiz de Los Mozos, I., Rájecký, M., Hluchý, M., Ule, J., and Blazek, D. (2020). CDK11 is required for transcription of replication-dependent histone genes. Nat Struct Mol Biol *27*, 500-510.

Galbraith, M.D., Bender, H., and Espinosa, J.M. (2019). Therapeutic targeting of transcriptional cyclin-dependent kinases. Transcription *10*, 118-136.

Huang, K.L., Jee, D., Stein, C.B., Elrod, N.D., Henriques, T., Mascibroda, L.G., Baillat, D., Russell, W.K., Adelman, K., and Wagner, E.J. (2020). Integrator Recruits Protein Phosphatase 2A to Prevent Pause Release and Facilitate Transcription Termination. Mol Cell *80*, 345-358.e349.

Ianevski, A., Giri, A.K., and Aittokallio, T. (2020). SynergyFinder 2.0: visual analytics of multi-drug combination synergies. Nucleic Acids Research *48*, W488-W493.

Kalan, S., Amat, R., Schachter, M.M., Kwiatkowski, N., Abraham, B.J., Liang, Y., Zhang, T., Olson, C.M., Larochelle, S., Young, R.A.*, et al.* (2017). Activation of the p53 Transcriptional Program Sensitizes Cancer Cells to Cdk7 Inhibitors. Cell Rep *21*, 467-481.

Kale, J., Osterlund, E.J., and Andrews, D.W. (2018). BCL-2 family proteins: changing partners in the dance towards death. Cell Death & Differentiation *25*, 65-80.
Kastenhuber, E.R., and Lowe, S.W. (2017). Putting p53 in Context. Cell *170*, 1062-1078.
Kluge, M., and Friedel, C.C. (2018). Watchdog - a workflow management system for the distributed analysis of large-scale experimental data. BMC bioinformatics *19*, 97.
Konopleva, M., Martinelli, G., Daver, N., Papayannidis, C., Wei, A., Higgins, B., Ott, M., Mascarenhas, J., and Andreeff, M. (2020). MDM2 inhibition: an important step forward in cancer therapy. Leukemia *34*, 2858-2874.
Krajewska, M., Dries, R., Grassetti, A.V., Dust, S., Gao, Y., Huang, H., Sharma, B., Day, D.S., Kwiatkowski, N., Pomaville, M.*, et al.* (2019). CDK12 loss in cancer cells affects DNA damage response genes through premature cleavage and polyadenylation. Nat Commun *10*, 1757.
Lawrence, M.S., Stojanov, P., Mermel, C.H., Robinson, J.T., Garraway, L.A., Golub, T.R., Meyerson, M., Gabriel, S.B., Lander, E.S., and Getz, G. (2014). Discovery and saturation analysis of cancer genes across 21 tumour types. Nature *505*, 495-501.
Leonard, D., Huang, W., Izadmehr, S., O'Connor, C.M., Wiredja, D.D., Wang, Z., Zaware, N., Chen, Y., Schlatzer, D.M., Kiselar, J.*, et al.* (2020). Selective PP2A Enhancement through Biased Heterotrimer Stabilization. Cell *181*, 688-701.e616.
Li, H., and Durbin, R. (2009). Fast and accurate short read alignment with Burrows-Wheeler transform. Bioinformatics *25*, 1754-1760.
Li, J., Zhi, X., Chen, S., Shen, X., Chen, C., Yuan, L., Guo, J., Meng, D., Chen, M., and Yao, L. (2020). CDK9 inhibitor CDKI-73 is synergetic lethal with PARP inhibitor olaparib in BRCA1 wide-type ovarian cancer. Am J Cancer Res *10*, 1140-1155.
Li, X., Huang, C.-H., Sánchez-Rivera, F.J., Kennedy, M.C., Tschaharganeh, D.F., Morris, J.P., Montinaro, A., O'Rourke, K.P., Banito, A., Wilkinson, J.E.*, et al.* (2022). A preclinical platform for assessing antitumor effects and systemic toxicities of cancer drug targets. *119*, e2110557119.
Li, Y., Yang, J., Aguilar, A., McEachern, D., Przybranowski, S., Liu, L., Yang, C.Y., Wang, M., Han, X., and Wang, S. (2019). Discovery of MD-224 as a First-in-Class, Highly Potent, and Efficacious Proteolysis Targeting Chimera Murine Double Minute 2 Degrader Capable of Achieving Complete and Durable Tumor Regression. Journal of medicinal chemistry *62*, 448-466.
Liao, Y., Smyth, G.K., and Shi, W. (2014). featureCounts: an efficient general purpose program for assigning sequence reads to genomic features. Bioinformatics *30*, 923-930.
Liberzon, A., Birger, C., Thorvaldsdóttir, H., Ghandi, M., Mesirov, J.P., and Tamayo, P. (2015). The Molecular Signatures Database (MSigDB) hallmark gene set collection. Cell Syst *1*, 417-425.
Lin, A., Giuliano, C.J., Palladino, A., John, K.M., Abramowicz, C., Yuan, M.L., Sausville, E.L., Lukow, D.A., Liu, L., Chait, A.R.*, et al.* (2019). Off-target toxicity is a common mechanism of action of cancer drugs undergoing clinical trials. Sci Transl Med *11*.
Longley, D.B., Harkin, D.P., and Johnston, P.G. (2003). 5-Fluorouracil: mechanisms of action and clinical strategies. Nature Reviews Cancer *3*, 330-338.
Lu, H., Xue, Y., Yu, G.K., Arias, C., Lin, J., Fong, S., Faure, M., Weisburd, B., Ji, X., Mercier, A.*, et al.* (2015). Compensatory induction of MYC expression by sustained CDK9 inhibition via a BRD4-dependent mechanism. Elife *4*, e06535.
Luyties, O., and Taatjes, D.J. (2022). The Mediator kinase module: an interface between cell signaling and transcription. Trends Biochem Sci *47*, 314-327.
Mandelker, D., Gabelli, S.B., Schmidt-Kittler, O., Zhu, J., Cheong, I., Huang, C.H., Kinzler, K.W., Vogelstein, B., and Amzel, L.M. (2009). A frequent kinase domain mutation that changes the interaction between PI3Kalpha and the membrane. Proc Natl Acad Sci U S A *106*, 16996-17001.
Minzel, W., Venkatachalam, A., Fink, A., Hung, E., Brachya, G., Burstain, I., Shaham, M., Rivlin, A., Omer, I., Zinger, A.*, et al.* (2018). Small Molecules Co-targeting CKIalpha and the Transcriptional Kinases CDK7/9 Control AML in Preclinical Models. Cell *175*, 171-185 e125.
Morales, F., and Giordano, A. (2016). Overview of CDK9 as a target in cancer research. Cell Cycle *15*, 519-527.
Moreno, N., Holsten, T., Mertins, J., Zhogbi, A., Johann, P., Kool, M., Meisterernst, M., and Kerl, K. (2017). Combined BRD4 and CDK9 inhibition as a new therapeutic approach in malignant rhabdoid tumors. Oncotarget *8*, 84986-84995.
Murtagh, F., and Legendre, P. (2014). Ward's Hierarchical Agglomerative Clustering Method: Which Algorithms Implement Ward's Criterion? Journal of Classification *31*, 274-295.

Olson, C.M., Jiang, B., Erb, M.A., Liang, Y., Doctor, Z.M., Zhang, Z., Zhang, T., Kwiatkowski, N., Boukhali, M., Green, J.L.*, et al.* (2018). Pharmacological perturbation of CDK9 using selective CDK9 inhibition or degradation. Nat Chem Biol *14*, 163-170.
Olson, C.M., Liang, Y., Leggett, A., Park, W.D., Li, L., Mills, C.E., Elsarrag, S.Z., Ficarro, S.B., Zhang, T., Duster, R.*, et al.* (2019). Development of a Selective CDK7 Covalent Inhibitor Reveals Predominant Cell-Cycle Phenotype. Cell Chem Biol *26*, 792-803 e710.
Parua, P.K., and Fisher, R.P. (2020). Dissecting the Pol II transcription cycle and derailing cancer with CDK inhibitors. Nature Chemical Biology *16*, 716-724.
Pemovska, T., Kontro, M., Yadav, B., Edgren, H., Eldfors, S., Szwajda, A., Almusa, H., Bespalov, M.M., Ellonen, P., Elonen, E.*, et al.* (2013). Individualized systems medicine strategy to tailor treatments for patients with chemorefractory acute myeloid leukemia. Cancer discovery *3*, 1416-1429.
Poon, E., Liang, T., Jamin, Y., Walz, S., Kwok, C., Hakkert, A., Barker, K., Urban, Z., Thway, K., Zeid, R.*, et al.* (2020). Orally bioavailable CDK9/2 inhibitor shows mechanism-based therapeutic potential in MYCN-driven neuroblastoma. The Journal of clinical investigation *130*, 5875-5892.
Porter, D.C., Farmaki, E., Altilia, S., Schools, G.P., West, D.K., Chen, M., Chang, B.D., Puzyrev, A.T., Lim, C.U., Rokow-Kittell, R.*, et al.* (2012). Cyclin-dependent kinase 8 mediates chemotherapy-induced tumor-promoting paracrine activities. Proc Natl Acad Sci U S A *109*, 13799-13804.
Potdar, S., Ianevski, A., Mpindi, J.P., Bychkov, D., Fiere, C., Ianevski, P., Yadav, B., Wennerberg, K., Aittokallio, T., Kallioniemi, O.*, et al.* (2020). Breeze: an integrated quality control and data analysis application for high-throughput drug screening. Bioinformatics *36*, 3602-3604.
Quereda, V., Bayle, S., Vena, F., Frydman, S.M., Monastyrskyi, A., Roush, W.R., and Duckett, D.R. (2019). Therapeutic Targeting of CDK12/CDK13 in Triple-Negative Breast Cancer. Cancer Cell *36*, 545-558 e547.
Robinson, M.D., McCarthy, D.J., and Smyth, G.K. (2010). edgeR: a Bioconductor package for differential expression analysis of digital gene expression data. Bioinformatics *26*, 139-140.
Singh, R., Letai, A., and Sarosiek, K. (2019). Regulation of apoptosis in health and disease: the balancing act of BCL-2 family proteins. Nature Reviews Molecular Cell Biology *20*, 175-193.
Štětková, M., Growková, K., Fojtík, P., Valčíková, B., Palušová, V., Verlande, A., Jorda, R., Kryštof, V., Hejret, V., Alexiou, P.*, et al.* (2020). CDK9 activity is critical for maintaining MDM4 overexpression in tumor cells. Cell death & disease *11*, 754.
Subramanian, A., Tamayo, P., Mootha Vamsi, K., Mukherjee, S., Ebert Benjamin, L., Gillette Michael, A., Paulovich, A., Pomeroy Scott, L., Golub Todd, R., Lander Eric, S.*, et al.* (2005). Gene set enrichment analysis: A knowledge-based approach for interpreting genome-wide expression profiles. Proceedings of the National Academy of Sciences *102*, 15545-15550.
Sur, S., Pagliarini, R., Bunz, F., Rago, C., Diaz, L.A., Jr., Kinzler, K.W., Vogelstein, B., and Papadopoulos, N. (2009). A panel of isogenic human cancer cells suggests a therapeutic approach for cancers with inactivated p53. Proceedings of the National Academy of Sciences of the United States of America *106*, 3964-3969.
Tait, S.W., and Green, D.R. (2013). Mitochondrial regulation of cell death. Cold Spring Harb Perspect Biol *5*.
Titov, D.V., Gilman, B., He, Q.L., Bhat, S., Low, W.K., Dang, Y., Smeaton, M., Demain, A.L., Miller, P.S., Kugel, J.F.*, et al.* (2011). XPB, a subunit of TFIIH, is a target of the natural product triptolide. Nat Chem Biol *7*, 182-188.
Tovar, C., Rosinski, J., Filipovic, Z., Higgins, B., Kolinsky, K., Hilton, H., Zhao, X., Vu, B.T., Qing, W., Packman, K.*, et al.* (2006). Small-molecule MDM2 antagonists reveal aberrant p53 signaling in cancer: implications for therapy. Proceedings of the National Academy of Sciences of the United States of America *103*, 1888-1893.
Vainonen Julia, P., Momeny, M., and Westermarck, J. (2021). Druggable cancer phosphatases. Science Translational Medicine *13*, eabe2967.
Vassilev, L.T., Vu, B.T., Graves, B., Carvajal, D., Podlaski, F., Filipovic, Z., Kong, N., Kammlott, U., Lukacs, C., Klein, C.*, et al.* (2004). In Vivo Activation of the p53 Pathway by Small-Molecule Antagonists of MDM2. *303*, 844-848.
Vervoort, S.J., Devlin, J.R., Kwiatkowski, N., Teng, M., Gray, N.S., and Johnstone, R.W. (2022). Targeting transcription cycles in cancer. Nature Reviews Cancer *22*, 5-24.

Vervoort, S.J., Welsh, S.A., Devlin, J.R., Barbieri, E., Knight, D.A., Offley, S., Bjelosevic, S., Costacurta, M., Todorovski, I., Kearney, C.J.*, et al.* (2021). The PP2A-Integrator-CDK9 axis fine-tunes transcription and can be targeted therapeutically in cancer. Cell *184*, 3143-3162.e3132.
Vos, S.M., Farnung, L., Boehning, M., Wigge, C., Linden, A., Urlaub, H., and Cramer, P. (2018a). Structure of activated transcription complex Pol II-DSIF-PAF-SPT6. Nature *560*, 607-612.
Vos, S.M., Farnung, L., Urlaub, H., and Cramer, P. (2018b). Structure of paused transcription complex Pol II-DSIF-NELF. Nature *560*, 601-606.
Wang, Y., Zhang, T., Kwiatkowski, N., Abraham, B.J., Lee, T.I., Xie, S., Yuzugullu, H., Von, T., Li, H., Lin, Z.*, et al.* (2015). CDK7-dependent transcriptional addiction in triple-negative breast cancer. Cell *163*, 174-186.
Yadav, B., Pemovska, T., Szwajda, A., Kulesskiy, E., Kontro, M., Karjalainen, R., Majumder, M.M., Malani, D., Murumägi, A., Knowles, J.*, et al.* (2014a). Quantitative scoring of differential drug sensitivity for individually optimized anticancer therapies. Sci Rep *4*, 5193-5193.
Yadav, B., Pemovska, T., Szwajda, A., Kulesskiy, E., Kontro, M., Karjalainen, R., Majumder, M.M., Malani, D., Murumägi, A., Knowles, J.*, et al.* (2014b). Quantitative scoring of differential drug sensitivity for individually optimized anticancer therapies. Sci Rep *4*, 5193.
Zanoni, M., Piccinini, F., Arienti, C., Zamagni, A., Santi, S., Polico, R., Bevilacqua, A., and Tesei, A. (2016). 3D tumor spheroid models for in vitro therapeutic screening: a systematic approach to enhance the biological relevance of data obtained. Sci Rep *6*, 19103.
Zhang, H., Pandey, S., Travers, M., Sun, H., Morton, G., Madzo, J., Chung, W., Khowsathit, J., Perez-Leal, O., Barrero, C.A.*, et al.* (2018). Targeting CDK9 Reactivates Epigenetically Silenced Genes in Cancer. Cell *175*, 1244-1258 e1226.
Zhang, T., Kwiatkowski, N., Olson, C.M., Dixon-Clarke, S.E., Abraham, B.J., Greifenberg, A.K., Ficarro, S.B., Elkins, J.M., Liang, Y., Hannett, N.M.*, et al.* (2016). Covalent targeting of remote cysteine residues to develop CDK12 and CDK13 inhibitors. Nat Chem Biol *12*, 876-884.
Zhou, Q., Li, T., and Price, D.H. (2012). RNA Polymerase II Elongation Control. Annual review of biochemistry *81*, 119-143.

ACKNOWLEDGMENTS

We thank Bert Vogelstein and Joaquin M. Espinosa for sharing HCT116 cell lines; Qiang Zhou for sharing i-CDK9; Nathaniel Gray for sharing THZ531, YLK-5-124, NVP-2, and SNS032-THAL inhibitors; Jukka Westermarck for sharing DT-061; FIMM High Content Imaging and Analysis unit for confocal imaging and analysis (HiLIFE, University of Helsinki and Biocenter Finland). This work was funded by Sigrid Juselius Foundation [4707979 to M.B.]; Cancer Society of Finland [4708690 to M.B.]; Academy of Finland [1309846 to M.B.]; Deutsche Forschungsgemeinschaft (DFG) [FR2938/9-1 to C.C.F.].

AUTHOR DECLARATION

The authors declare no competing interests.

FIGURES AND FIGURE LEGENDS

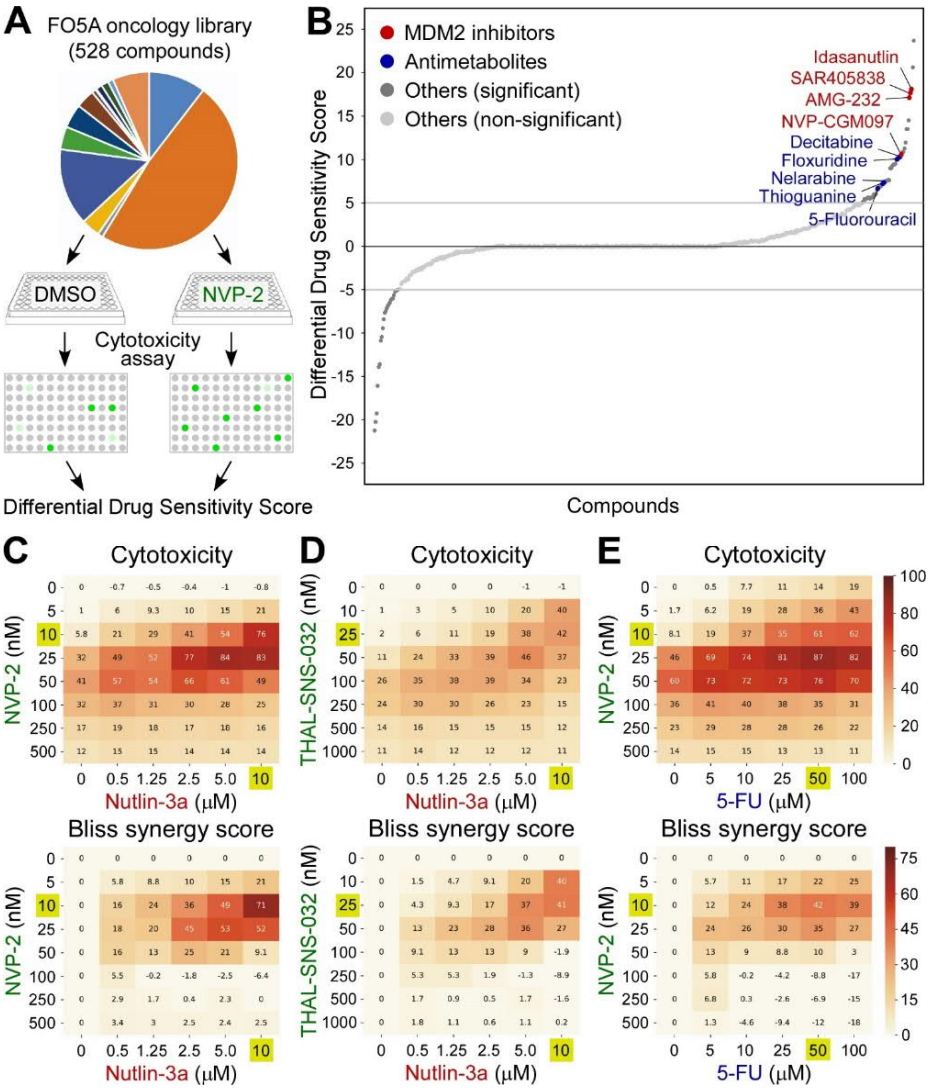

Figure 1. MDM2 inhibitors and antimetabolites are synthetic-lethal with selective perturbation of P-TEFb.

(A) Workflow of the FO5A oncology library screen. DMSO- and NVP-2-treated HCT116 cells were exposed to the library compounds at five concentrations for 72 hours, after which cytotoxicity was measured using CellTox Green assay and dDSS values were calculated. Green dots indicate fluorescence readouts of specific FO5A library compound combinations.

(B) Waterfall plot representing results of the screen. Compounds with dDSS values ≥ 5 and ≤ -5 were considered as significant (dark grey). MDM2 inhibitors (red) and antimetabolites (blue) are highlighted.

(C-E) 8 × 6 cytotoxicity matrices with combinatorial titrations of NVP-2 and THAL-SNS-032 (green) with Nutlin-3a (red) and 5-Fluorouracil (5-FU; blue) at indicated doses to test for the synthetic lethality of compounds in HCT116 cells, depicting cytotoxicity (top) and synergy (bottom) of the combinations. Cytotoxicity values obtained at 48 hr of the treatments using CellTox Green assay were normalized to the DMSO control and are presented as percentages of the maximum cytotoxicity which was set at 100 %. Results represent the average of independent experiments (n = 3). Combinations with the highest Bliss synergy scores are highlighted (gold).

See also Figure S1.

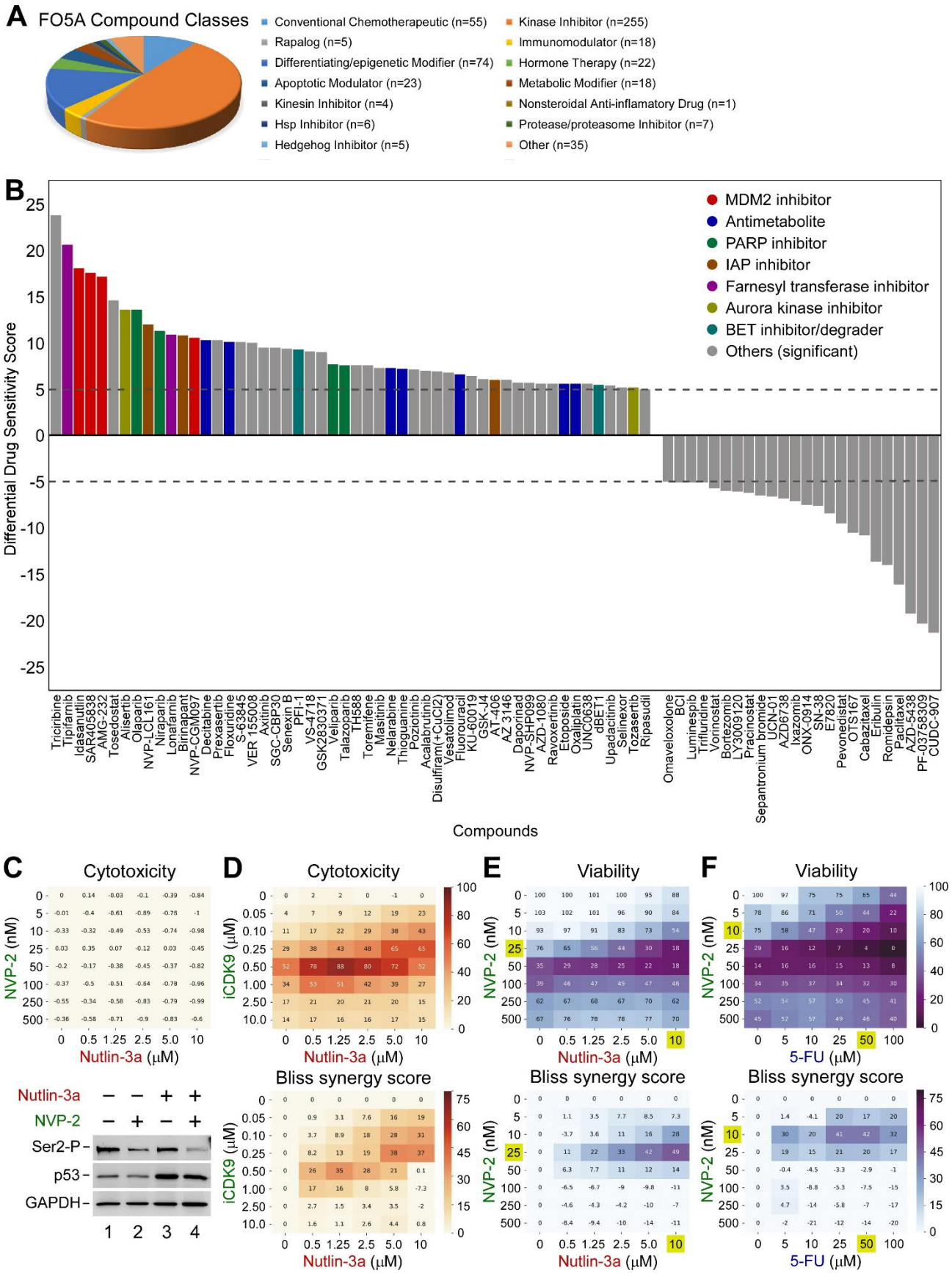
A
FO5A Compound Classes
Conventional Chemotherapeutic (n=55)
Kinase Inhibitor (n=255)
Rapalog (n=5)
Immunomodulator (n=18)
Differentiating/epigenetic Modifier (n=74)
Hormone Therapy (n=22)
Apoptotic Modulator (n=23)
Metabolic Modifier (n=18)
Kinesin Inhibitor (n=4)
Nonsteroidal Anti-inflamatory Drug (n=1)
Hsp Inhibitor (n=6)
Protease/proteasome Inhibitor (n=7)
Hedgehog Inhibitor (n=5)
Other (n=35)
B
MDM2 inhibitor
Antimetabolite
PARP inhibitor
IAP inhibitor
Farnesyl transferase inhibitor
Aurora kinase inhibitor
BET inhibitor/degrader
Others (significant)
Differential Drug Sensitivity Score
Compounds
C
Cytotoxicity
NVP-2 (nM)
Nutlin-3a (μM)
Nutlin-3a
NVP-2
Ser2-P
p53
GAPDH
1 2 3 4
D
Cytotoxicity
iCDK9 (μM)
Nutlin-3a (μM)
Bliss synergy score
E
Viability
NVP-2 (nM)
Nutlin-3a (μM)
Bliss synergy score
F
Viability
NVP-2 (nM)
5-FU (μM)
Bliss synergy score

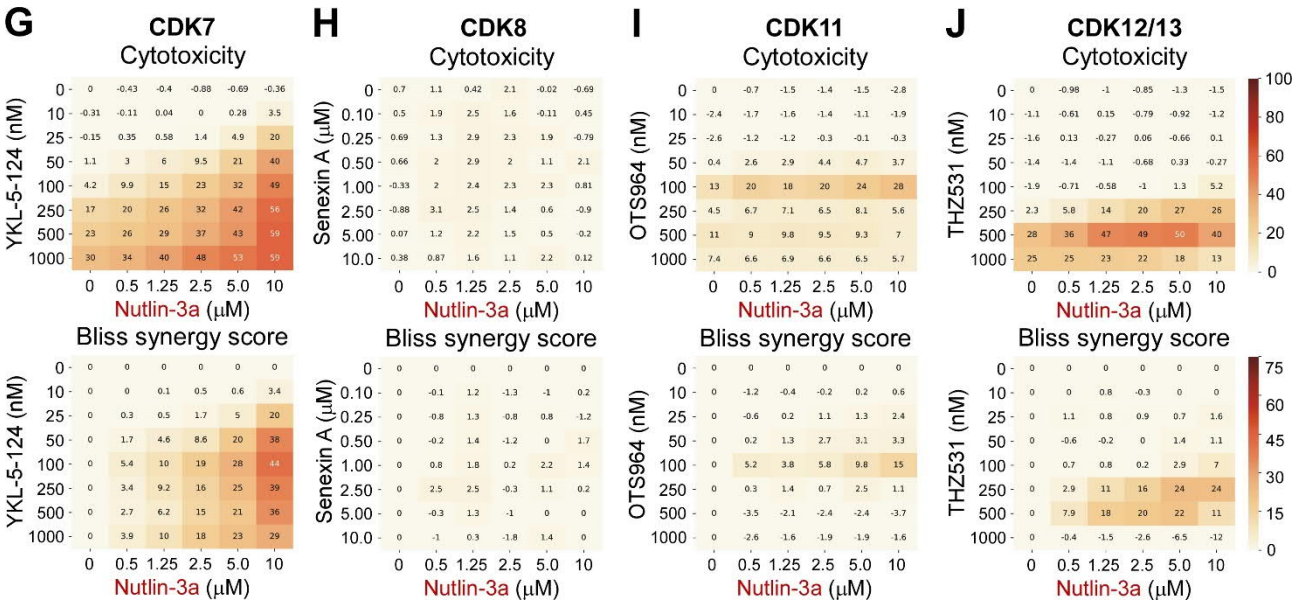

Figure S1. Selective inhibition of CDK7 and P-TEFb but not other tCDKs is synthetic-lethal with MDM2 inhibitor Nutlin-3a.

(A) Compound classes of the FO5A oncology library. Pie chart represents classes of investigational and clinical anti-cancer compounds listed on the right.

(B) Waterfall plot representing results of the screen. Compounds with dDSS values ≥ 5 and ≤ -5 were considered as significant and depicted according to the legend on the right.

(C) (Top) 8 × 6 cytotoxicity matrix with combinatorial titrations of NVP-2 (green) with Nutlin-3a (red) at indicated doses in non-transformed CCD 841 CoN colon epithelial cells. Cytotoxicity values obtained at 48 hr of the treatments using CellTox Green assay were normalized to the DMSO control and are presented as percentages of the maximum cytotoxicity which was set at 100 %. Results represent the average of independent experiments (n = 3). (Bottom) CCD 841 CoN cells were treated with the indicated combinations of NVP-2 (10 nM) and Nutlin-3a (10 μM) for 8 hr prior to preparation of whole cell extracts and detection of the indicated proteins by Western blotting.

(D, G-J) 8 × 6 matrices with combinatorial titrations of iCDK9 (green) and the indicated tCDK inhibitors (black) with Nutlin-3a (red) at indicated doses to test for the synthetic lethality of compounds in HCT116 cells, depicting cytotoxicity (top) and synergy (bottom) of the combinations. Targeted tCDKs are indicated on top. Cytotoxicity values obtained at 48 hr of the treatments using CellTox Green assay were normalized to the DMSO control and are presented as percentages of the maximum cytotoxicity which was set at 100 %. Results represent the average of independent experiments (n = 3).

(E,F) 8 × 6 matrices with combinatorial titrations of NVP-2 (green) with Nutlin-3a (red) and 5-Fluorouracil (5-FU; blue) at indicated doses to test for the synthetic lethality of compounds in HCT116 cells, depicting viability (top) and synergy (bottom) of the combinations. Viability values obtained at 48 hr of the treatments using CellTiter-Glo assay were normalized to the DMSO control and are presented as percentages of the maximum viability which was set at 100 %. Results represent the average of independent experiments (n = 3). Combinations with the highest Bliss synergy scores in HCT116 TP53 $^{+/+}$ cells are highlighted (gold).

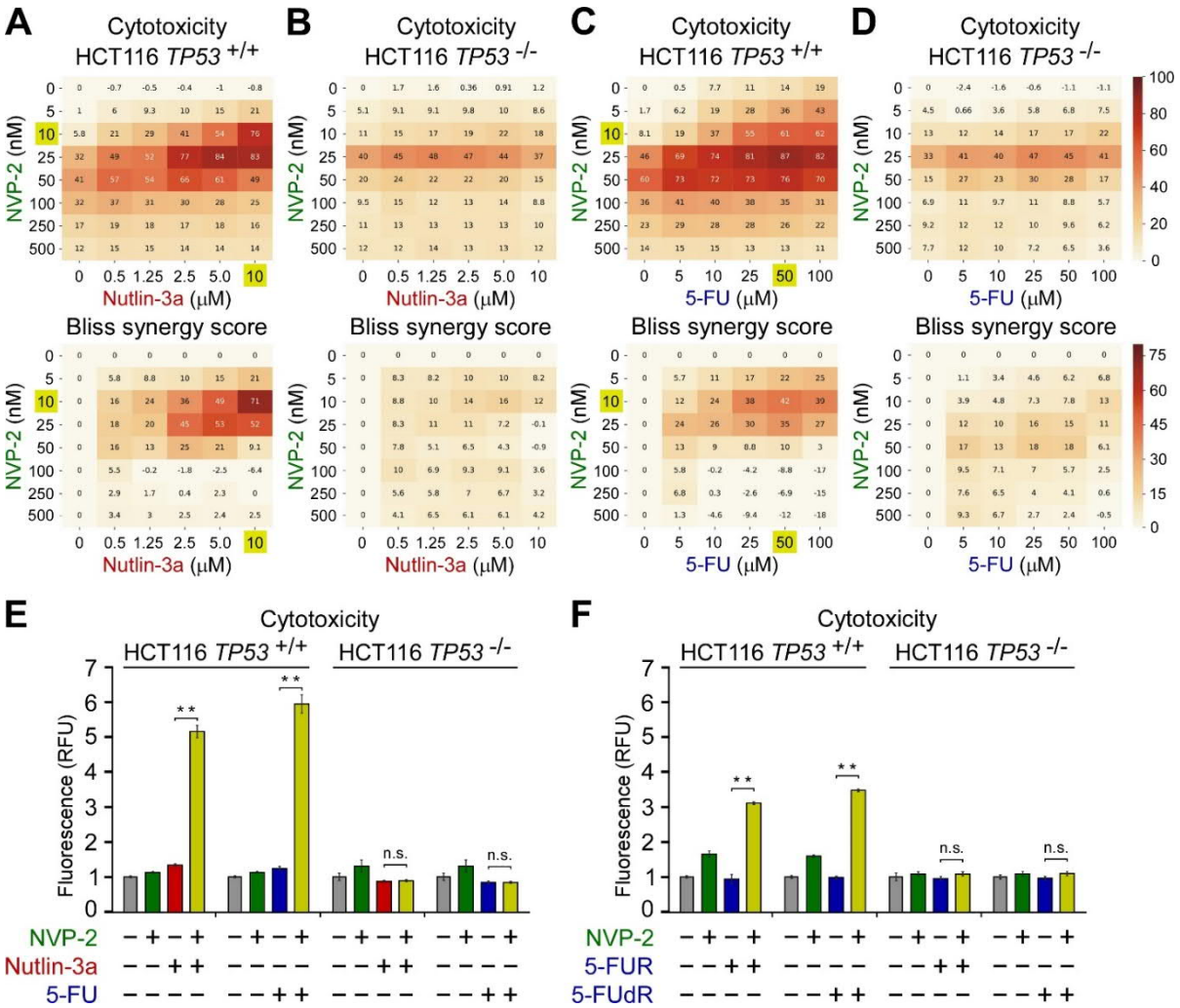

Figure 2. Synthetic lethality of P-TEFb inhibitor NVP-2 with MDM2 inhibitor Nutlin-3a and antimetabolites is p53-dependent.

(A-D) 8 × 6 matrices with combinatorial titrations of NVP-2 (green) with Nutlin-3a (red) and 5-Fluorouracil (5-FU; blue) at indicated doses to test for the synthetic lethality of compounds in HCT116 *TP53* $^{+/+}$ and HCT116 *TP53* $^{-/-}$ cells, depicting cytotoxicity (top) and synergy (bottom) of the combinations. Cytotoxicity values obtained at 48 hr of the treatments using CellTox Green assay were normalized to the DMSO control and are presented as percentages of the maximum cytotoxicity which was set at 100 %. Results represent the average of independent experiments (n = 3). Combinations with the highest Bliss synergy scores in HCT116 TP53 $^{+/+}$ cells are highlighted (gold).

(E,F) Cytotoxicity of HCT116 *TP53* $^{+/+}$ and HCT116 *TP53* $^{-/-}$ cells treated with the DMSO control (grey), NVP-2 (10 nM; green), Nutlin-3a (10 μM; red), and antimetabolites 5-Fluorouracil (5-FU; 50 μM), 5-fluorouridine (5-FUR; 0.5 μM) and 5-fluorodeoxyuridine (5-FUdR; 0.15 μM) (blue) alone and in combination (gold) as indicated for 48 hr measured using CellTox Green assay. Results are presented as fluorescence values relative to the DMSO control and plotted as the mean ± s.e.m. (n = 3). **, P < 0.01; n.s., non-significant, determined by Student's *t* test.

See also Figure S2.

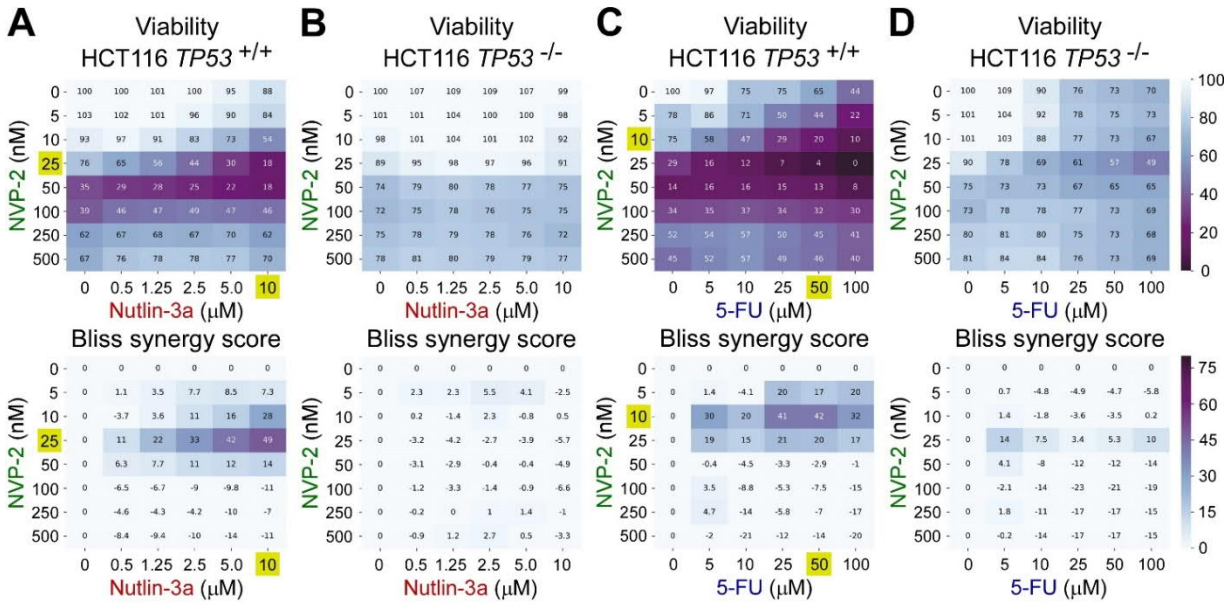

Figure S2. Synthetic lethality of P-TEFb inhibitor NVP-2 with MDM2 inhibitor Nutlin-3a and antimetabolite 5-FU is p53-dependent.

(A-D) 8 × 6 matrices with combinatorial titrations of NVP-2 (green) with Nutlin-3a (red) and 5-Fluorouracil (5-FU; blue) at indicated doses to test for the synthetic lethality of compounds in HCT116 *TP53* $^{+/+}$ and HCT116 *TP53* $^{-/-}$ cells, depicting viability (top) and synergy (bottom) of the combinations. Viability values obtained at 48 hr of the treatments using CellTiter-Glo assay were normalized to the DMSO control and are presented as percentages of the maximum viability which was set at 100 %. Results represent the average of independent experiments (n = 3). Combinations with the highest Bliss synergy scores in HCT116 TP53 $^{+/+}$ cells are highlighted (gold).

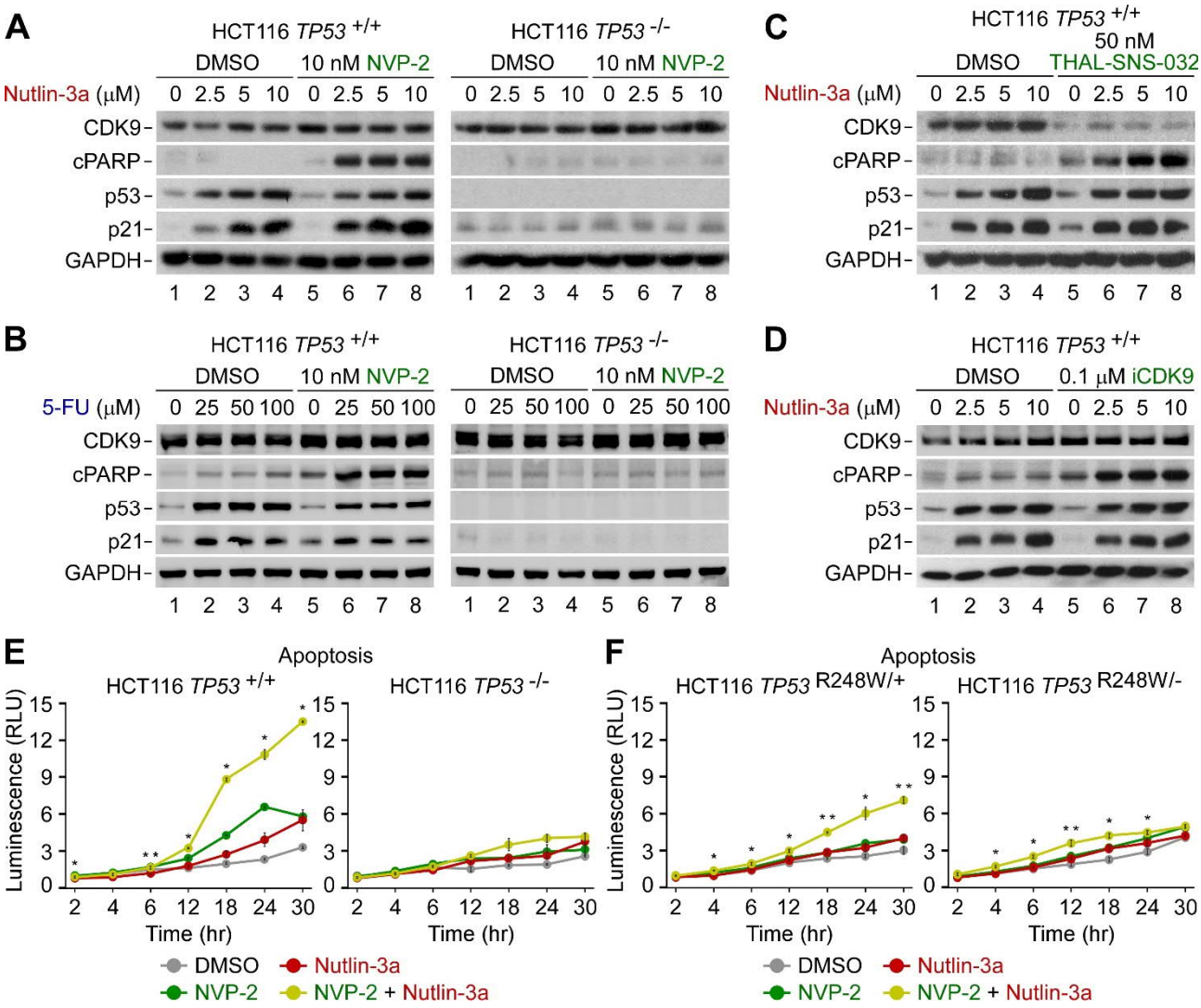

Figure 3. Activation of apoptosis underlies p53-dependent synthetic lethality of p53 activation and P-TEFb inhibition.

(A-D) HCT116 *TP53* $^{+/+}$ and HCT116 *TP53* $^{-/-}$ cells were treated with DMSO and indicated combinations and doses of P-TEFb antagonists (green), Nutlin-3a (red), and 5-Fluorouracil (5-FU; blue) for 24 hr prior to preparation of whole cell extracts and detection of the indicated proteins by Western blotting.

(E,F) Apoptosis of the indicated HCT116 cell lines treated with DMSO (grey), NVP-2 (10 nM; green) and Nutlin-3a (10 μM; red) alone and in combination (gold). Results obtained at the time points indicated below the graphs using RealTime-Glo Annexin V assay are presented as luminescence values relative to the DMSO control values at 2 hr and plotted as the mean ± s.e.m. (n = 3). *, $P < 0.05$; **, $P < 0.01$, determined by Student's *t* test using Nutlin-3a and Nutlin-3a + NVP-2 data sets.

See also Figure S3.

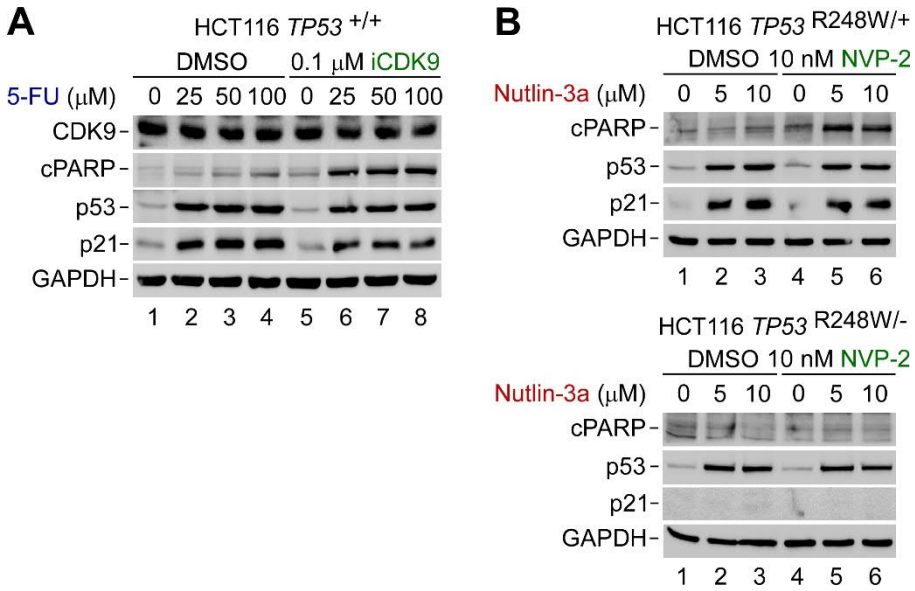

Figure S3. Activation of apoptosis underlies p53-dependent synthetic lethality of CDK9 inhibition and p53 activation.

(A,B) HCT116 *TP53* $^{+/+}$, HCT116 *TP53* $^{R248W/+}$ and HCT116 *TP53* $^{R248W/-}$ cells were treated with DMSO and indicated combinations and doses of CDK9 inhibitors (green), Nutlin-3a (red), and 5-Fluorouracil (5-FU; blue) for 24 hr prior to preparation of whole cell extracts and detection of the indicated proteins by Western blotting.

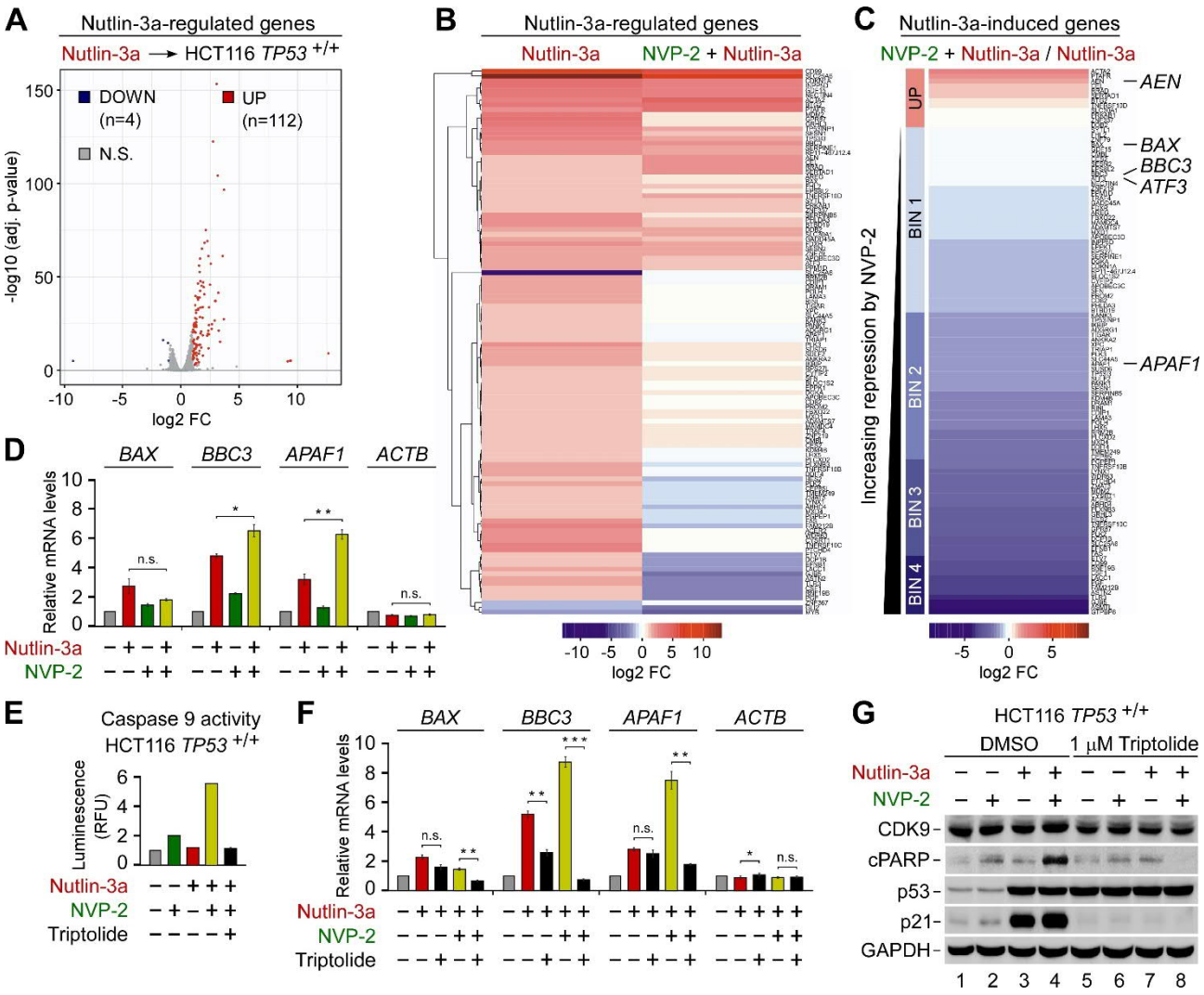

Figure 4. Transcriptional induction of NVP-2-insensitive pro-apoptotic genes is required for the synthetic lethality of p53 activation and P-TEFb inhibition.

(A) Volcano plot representation of differentially expressed protein-coding genes (n = 116; p-adj ≤ 0.001; Log2 FC ≥ 1) from RNA-seq experiments (n = 3) of HCT116 *TP53* $^{+/+}$ cells treated with DMSO and 10 μM of Nutlin-3a for eight hours. Down-regulated, up-regulated and non-significantly regulated (N.S.) genes are shown as blue, red and grey dots, respectively. FC, fold-change.

(B) Hierarchically clustered heatmap representation of Nutlin-3a-regulated protein-coding genes (n = 116; p-adj ≤ 0.001; Log2 FC ≥ 1) from RNA-seq experiments (n = 3) of HCT116 *TP53* $^{+/+}$ cells treated with 10 μM of Nutlin-3a alone and in combination with 20 nM of NVP-2 for eight hours. Rows represent Log2 FC values of each gene under the depicted treatments on top relative to the DMSO control treatment. FC, fold-change.

(C) Heatmap representation of Nutlin-3a-induced protein-coding genes (n = 112; p-adj ≤ 0.001; Log2 FC ≥ 1) from RNA-seq experiments (n = 3) in HCT116 *TP53* $^{+/+}$ cells treated with 10 μM of Nutlin-3a alone and in combination with 20 nM of NVP-2 for eight hours. Rows represent Log2 FC values of each gene under the Nutlin-3a + NVP-2 combination treatment relative to the DMSO control treatment. Genes are sorted from largest to smallest Log2 FC values. UP labels genes induced by NVP-2 (Log2 FC >0). BIN 1 (0 > Log2 FC >= -1), BIN 2 (-1 > Log2 FC >= -2), BIN 3 (-2 > Log2 FC >= -3) and BIN 4 (Log2 FC <-3) labels genes repressed by NVP-2. FC, fold-change.

(D) HCT116 *TP53* $^{+/+}$ cells were treated with DMSO (grey), Nutlin-3a (10 μM; red) and NVP-2 (10 nM; green) alone and in combination (gold) as indicated for 24 hr prior to quantifying mRNA levels

of the indicated genes with RT-qPCR. Results normalized to the *GAPDH* RNA levels and DMSO control are presented as the mean ± s.e.m. (n = 3). *, P < 0.05; **, P < 0.01; n.s., non-significant, determined by Student's *t* test.

(E) Activity of Caspase 9 measured using Caspase-Glo 9 assay in whole cell extracts of HCT116 *TP53* $^{+/+}$ cells treated with DMSO (grey), NVP-2 (10 nM; green) and Nutlin-3a (10 μM; red) alone and in combination (gold), and Triptolide (1 μM; black) as indicated for 30 hr. Results are presented as luminescence values relative to the DMSO control and plotted as the mean ± s.e.m. (n = 1).

(F) HCT116 *TP53* $^{+/+}$ cells were treated with DMSO (grey), Nutlin-3a alone (10 μM; red) and in combination with NVP-2 (10 nM; gold), and Triptolide (1 μM; black) as indicated for 24 hr prior to quantifying mRNA levels of the indicated genes with RT-qPCR. Results normalized to the *GAPDH* mRNA levels and DMSO control are presented as the mean ± s.e.m. (n = 3). *, P < 0.05; **, P < 0.01; ***, P < 0.001; n.s., non-significant, determined by Student's *t* test.

(G) HCT116 *TP53* $^{+/+}$ cells treated with indicated combinations of NVP-2 (10 nM; green) and Nutlin-3a (10 μM; red) were co-treated with DMSO and Triptolide as indicated for 24 hr prior to preparation of whole cell extracts and detection of the indicated proteins by Western blotting.

See also Figure S4.

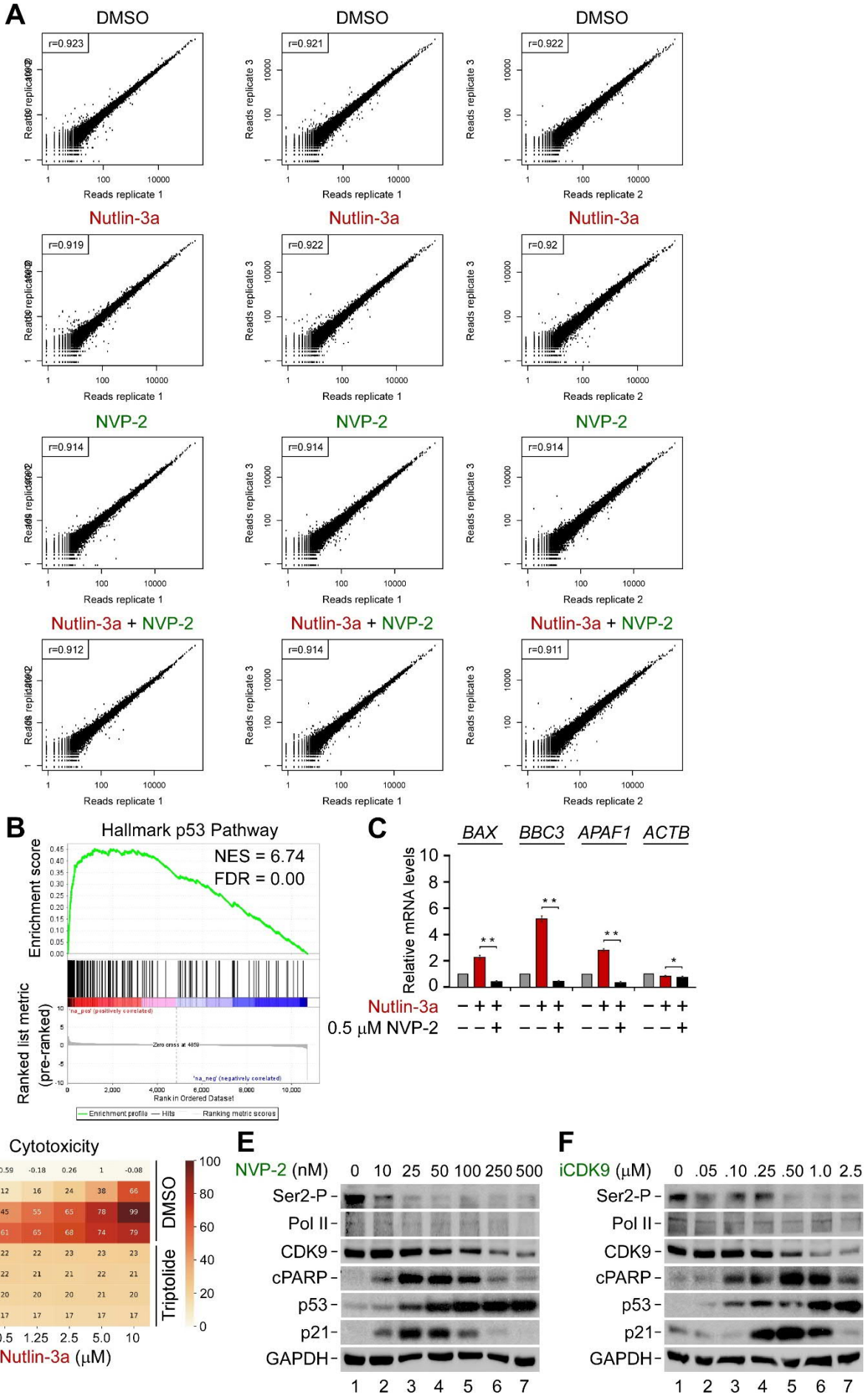
A
DMSO
r=0.923
r=0.921
r=0.922
Nutlin-3a
r=0.919
r=0.922
r=0.92
NVP-2
r=0.914
r=0.914
r=0.914
Nutlin-3a + NVP-2
r=0.912
r=0.914
r=0.911
Reads replicate 1
Reads replicate 2
Reads replicate 3
B
Hallmark p53 Pathway
NES = 6.74
FDR = 0.00
Enrichment score
Ranked list metric (pre-ranked)
Rank in Ordered Dataset
C
BAX
BBC3
APAF1
ACTB
Relative mRNA levels
Nutlin-3a
0.5 μM NVP-2
D
Cytotoxicity
NVP-2 (nM)
DMSO
Triptolide
Nutlin-3a (μM)
E
NVP-2 (nM) 0 10 25 50 100 250 500
Ser2-P
Pol II
CDK9
cPARP
p53
p21
GAPDH
1 2 3 4 5 6 7
F
iCDK9 (μM) 0 .05 .10 .25 .50 1.0 2.5
Ser2-P
Pol II
CDK9
cPARP
p53
p21
GAPDH
1 2 3 4 5 6 7

Figure S4. Transcriptional induction of NVP-2-insensitive pro-apoptotic genes is required for the synthetic lethality of p53 activation and P-TEFb inhibition.

(A) Scatterplots comparing raw read counts of all annotated genes from RNA-seq data sets (n = 3) are shown and spearman correlation (r) is indicated. HCT116 cells were treated for eight hours as indicated on top of each graph.

(B) Gene set enrichment analysis (GSEA) of the protein-coding gene data set regulated by Nutlin-3a. The top gene set is shown. NES, normalized enrichment score. FDR, false discovery rate.

(C,D) HCT116 *TP53* $^{+/+}$ cells were treated with the DMSO control and increasing doses of NVP-2 and iCDK9 (green) for 24 hr prior to preparation of whole cell extracts and detection of the indicated proteins by Western blotting.

(E) 4 × 6 cytotoxicity matrices with combinatorial titrations of Nutlin-3a (red) with NVP-2 (green) at indicated doses in HCT116 cells. Cells were co-treated with DMSO and Triptolide (1 μM) as indicated. Cytotoxicity values obtained at 48 hr of the treatments using CellTox Green assay were normalized to the DMSO control and are presented as percentages of the maximum cytotoxicity which was set at 100 %.

(F) HCT116 *TP53* $^{+/+}$ cells were treated with DMSO (grey), Nutlin-3a (10 μM; red) and NVP-2 (0.5 μM; black) as indicated for 24 hr prior to quantifying mRNA levels of the indicated genes with RT-qPCR. Results normalized to the *GAPDH* mRNA levels and DMSO control are presented as the mean ± s.e.m. (n = 3). **, $P < 0.01$, determined by Student's *t* test.

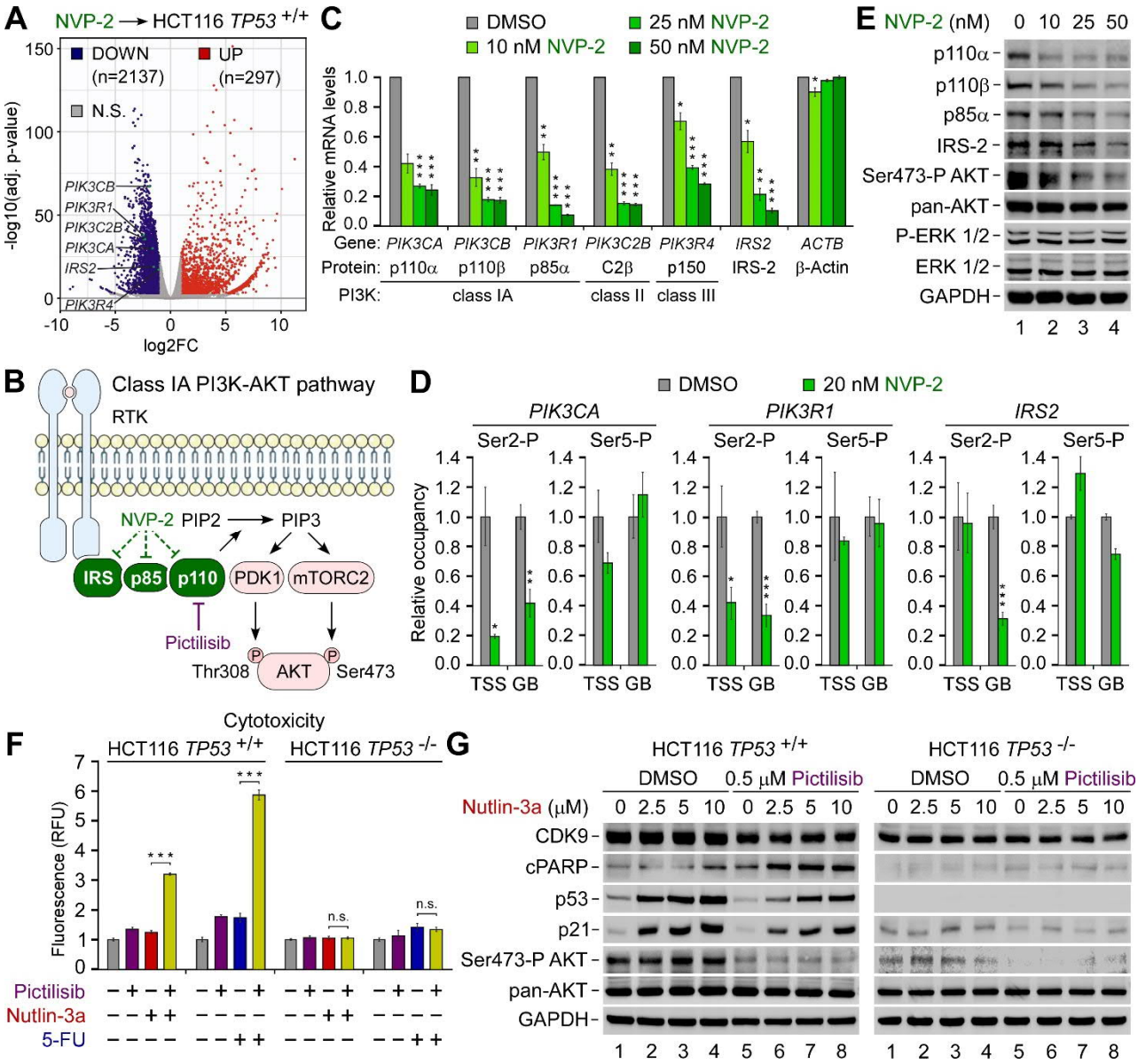

Figure 5. Repression of P-TEFb-dependent genes encoding key components of the pro-survival PI3K-AKT pathway contributes to the synthetic lethality of p53 activation and P-TEFb inhibition.

(A) Volcano plot representation of differentially expressed protein-coding genes (p-adj ≤ 0.001; Log2 FC ≥ 1) from RNA-seq experiments (n = 3) of HCT116 *TP53* $^{+/+}$ cells treated with DMSO and 20 nM of NVP-2 for eight hours. Down-regulated (DOWN), up-regulated (UP) and non-significantly regulated (N.S.) genes are shown as blue, red and grey dots, respectively. FC, fold-change.

(B) Cartoon depicting Class IA PI3K-AKT pathway. Ligand-induced activation of transmembrane receptor tyrosine kinase (RTK; blue) results in autophosphorylation on tyrosine residues, recruiting the PI3K catalytic subunit p110α/β/δ to the membrane via PI3K regulatory subunits, such as p85α, of which SH2 domains bind phosphotyrosyl residues on RTKs or adaptor proteins, e.g. IRS-2. Allosterically activated, PI3K phosphorylates phosphatidylinositol 4,5-bisphosphate (PtdIns(4,5)P_2; PIP2) to produce phosphatidylinositol 3,4,5-trisphosphate (PtdIns(3,4,5)P_3; PIP3). PIP3 acts as a second messenger to recruit the serine/threonine protein kinase AKT to the plasma membrane alongside phosphoinositide-dependent kinase-1 (PDK-1) and mechanistic target of rapamycin complex 2 (mTORC2), which activate AKT fully by phosphorylating Thr308 and Ser473, respectively. Green dashed lines denote transcriptional repression of genes encoding IRS-2, p85α and p110 by NVP-2. Pharmacological targeting of p110α/β/δ by the class Ia PI3K inhibitor Pictilisib is in magenta.

(C) HCT116 *TP53* $^{+/+}$ cells were treated with DMSO (grey) and increasing doses of NVP-2 (green) for 8 hr prior to quantifying mRNA levels of the indicated genes with RT-qPCR. Proteins encoded by the genes and their PI3K protein family classes are indicated. Results were normalized to the *GAPDH* mRNA levels and DMSO control, and are presented as the mean ± s.e.m. (n = 3). *, P < 0.05; **, P < 0.01; ***, P < 0.001, determined by Student's *t* test.

(D) HCT116 *TP53* $^{+/+}$ cells were treated with DMSO (grey) and NVP-2 (20 nM; green) for 3 hr prior to determining the levels of Ser2-P and Ser5-P forms relative to total Pol II at transcription start site (TSS) and gene body (GB) of the indicated PI3K-AKT pathway genes with ChIP-qPCR. Results were normalized to the DMSO control values that were set to 1 and are presented as the mean ± s.e.m. (n = 2). *, P < 0.05; **, P < 0.01; ***, P < 0.001, determined by Student's *t* test.

(E) HCT116 *TP53* $^{+/+}$ cells were treated with DMSO and increasing doses of NVP-2 (green) for 24 hr prior to preparation of whole cell extracts and detection of the indicated proteins by Western blotting.

(F) Cytotoxicity of HCT116 *TP53* $^{+/+}$ and HCT116 *TP53* $^{-/-}$ cells treated with DMSO (grey), Pictilisib (1 μM; magenta), Nutlin-3a (10 μM; red), and 5-Fluorouracil (5-FU; 25 μM) (blue) alone and in combination (gold) as indicated for 48 hr measured using CellTox Green assay. Results are presented as fluorescence values relative to the DMSO control and plotted as the mean ± s.e.m. (n = 3). ***, P < 0.001; n.s., non-significant, determined by Student's *t* test.

(G) HCT116 *TP53* $^{+/+}$ and HCT116 *TP53* $^{-/-}$ cells were treated with DMSO and indicated combinations and doses of Pictilisib (magenta) and Nutlin-3a (red) for 24 hr prior to preparation of whole cell extracts and detection of the indicated proteins by Western blotting.

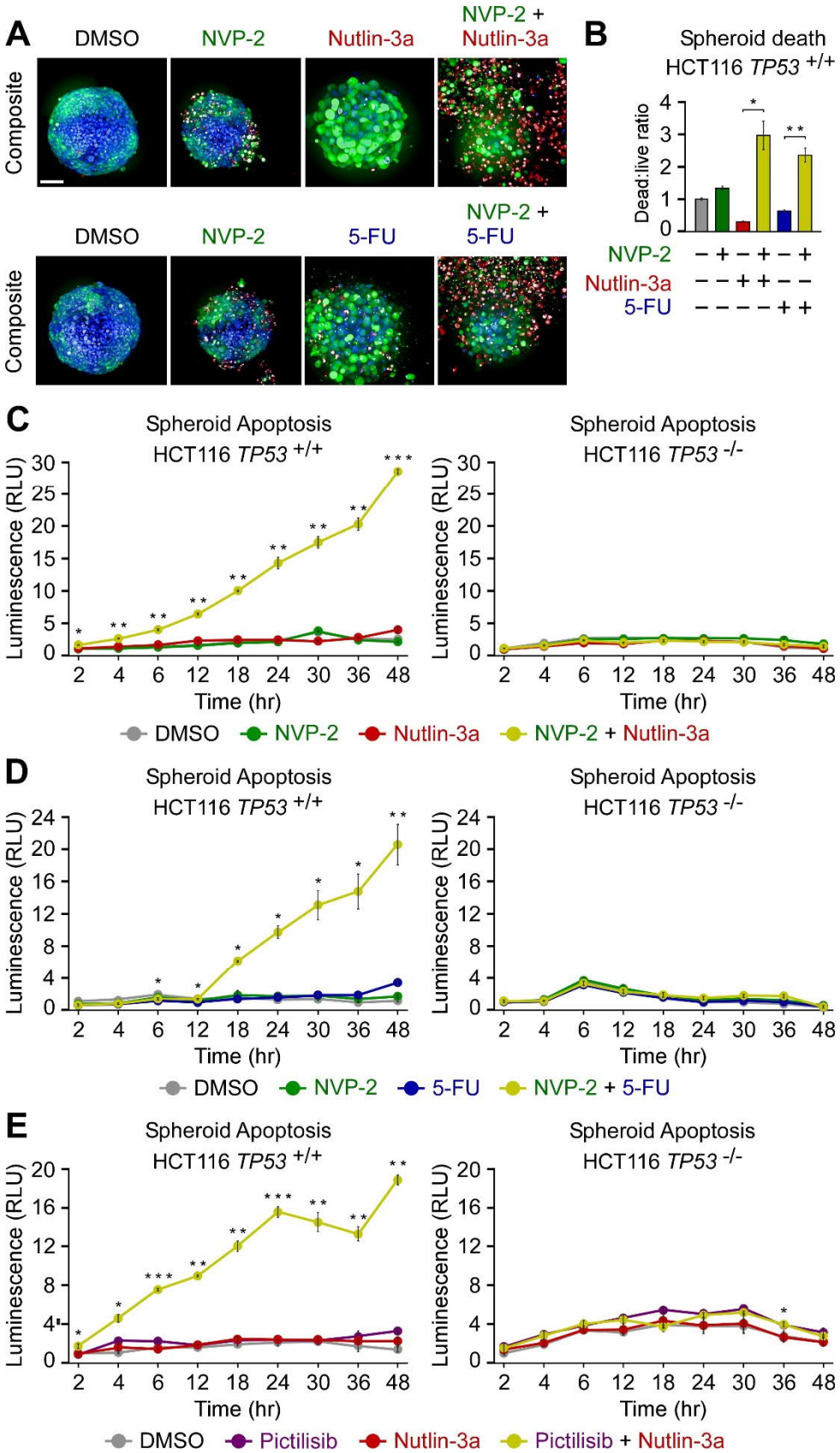

Figure 6. Synthetic lethality of p53 activation and P-TEFb inhibition remains effectual in spheroid culture system.

(A) Representative composite images of HCT116 *TP53* $^{+/+}$ spheroid cultures treated with DMSO, NVP-2 (10 nM), Nutlin-3a (10 μM), and 5-Fluorouracil (5-FU; 25 μM) alone and in the combinations as indicated. Spheroids were formed for 48 hr, exposed to the treatments for 96 hr and stained with

Calcein AM (1 μM), DRAQ7 (6 μM), and Hoechst (1x) prior to confocal microscopy imaging. Scale bar, 100 μm.

(B) Quantification of death of HCT116 *TP53* $^{+/+}$ spheroid cultures treated with DMSO, NVP-2 (10 nM), Nutlin-3a (10 μM), and 5-Fluorouracil (5-FU; 25 μM) alone and in the combinations as indicated. Death of spheroids was determined as a ratio of integrated intensities from Calcein AM and DRAQ7 staining in segmented cells normalized to the total spheroid cell number quantified by Hoechst staining (dead:live ratio). The results are presented as dead:live ratio values relative to the DMSO control values and plotted as the mean ± s.e.m. (n = 3). *, $P < 0.05$; **, $P < 0.01$, determined by Student's *t* test using Nutlin-3a and Nutlin-3a + NVP-2, and 5-FU and 5-FU + NVP-2 data sets.

(C-E) Apoptosis of HCT116 *TP53* $^{+/+}$ and HCT116 *TP53* $^{-/-}$ cell spheroid cultures treated with DMSO (grey), NVP-2 (10 nM; green), Nutlin-3a (10 μM; red), 5-Fluorouracil (5-FU; 25 μM) (blue) and Pictilisib (0.5 μM; magenta) alone and in combination (gold). Spheroids were formed for 48 hr prior to the treatments. Results obtained at the time points indicated below the graphs using RealTime-Glo Annexin V assay are presented as luminescence values relative to the DMSO control values at 2 hr and plotted as the mean ± s.e.m. (n = 3). *, $P < 0.05$; **, $P < 0.01$; ***, $P < 0.001$, determined by Student's *t* test using Nutlin-3a and Nutlin-3a + NVP-2 (C), 5-FU and 5-FU + NVP-2 (D), and Nutlin-3a and Nutlin-3a + Pictilisib (E) data sets.

See also Figure S5.

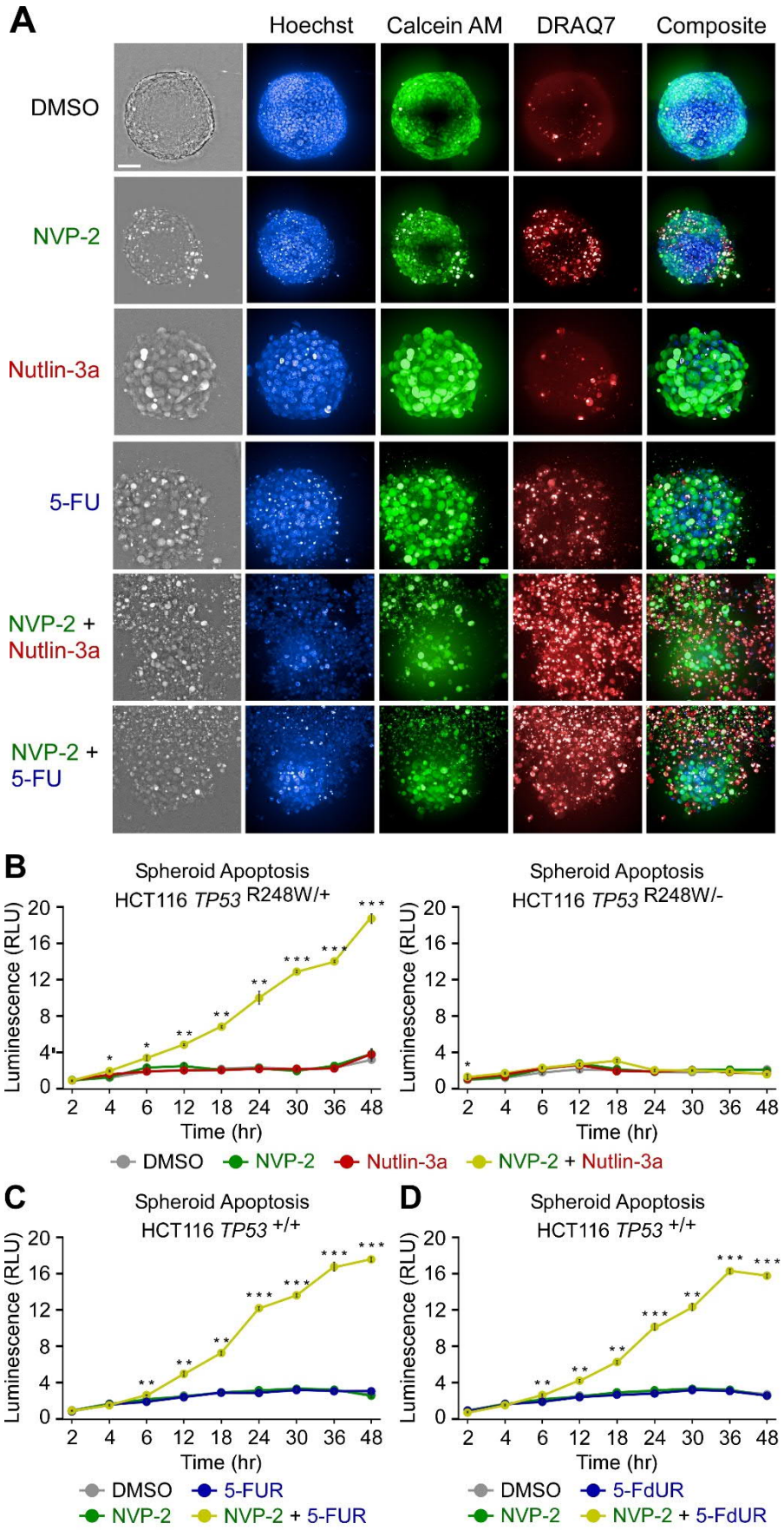
A
Hoechst
Calcein AM
DRAQ7
Composite
DMSO
NVP-2
Nutlin-3a
5-FU
NVP-2 +
Nutlin-3a
NVP-2 +
5-FU
B
Spheroid Apoptosis
HCT116 TP53 R248W/+
Spheroid Apoptosis
HCT116 TP53 R248W/-
Luminescence (RLU)
Time (hr)
DMSO
NVP-2
Nutlin-3a
NVP-2 + Nutlin-3a
C
Spheroid Apoptosis
HCT116 TP53 +/+
DMSO
5-FUR
NVP-2
NVP-2 + 5-FUR
D
Spheroid Apoptosis
HCT116 TP53 +/+
DMSO
5-FdUR
NVP-2
NVP-2 + 5-FdUR

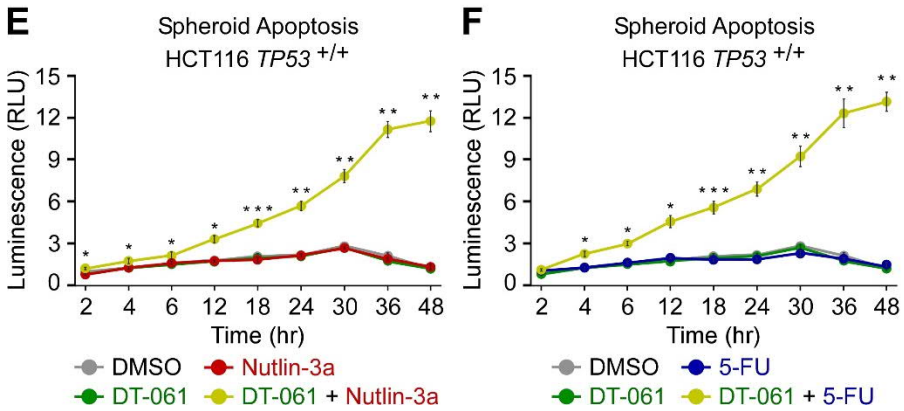

Figure S5. Synthetic lethality of p53 activation and P-TEFb inhibition remains effectual in spheroid culture system.

(A) Representative images of HCT116 *TP53* $^{+/+}$ spheroid cultures treated with DMSO, Nutlin-3a (10 μM), NVP-2 (10 nM), and 5-Fluorouracil (5-FU; 25 μM) alone and in the combinations as indicated. Spheroids were formed for 48 hr, exposed to the treatments for 96 hr and stained with a mixture Calcein AM (1 μM), DRAQ7 (6 μM) and Hoechst (1x) prior to confocal microscopy imaging. Composite images of all three staining are shown on the right. Scale bar, 100 μm.

(B-F) Apoptosis of the indicated HCT116 *TP53*$^{R248W/+}$, HCT116 *TP53*$^{R248W/-}$ and HCT116 *TP53* $^{+/+}$ cell spheroid cultures treated with DMSO (grey), Nutlin-3a (10 μM; red), NVP-2 (10 nM; green), 5-fluorouridine (5-FUR; 0.5 μM) and 5-fluorodeoxyuridine (5-FUdR; 0.15 μM), 5-Fluorouracil (5-FU; 25 μM) and DT-061 (10 μM; green) alone and in the indicated combinations (gold). Spheroids were formed for 48 hr prior to the treatments. Results obtained at the time points indicated below the graphs using RealTime-Glo Annexin V assay are presented as luminescence values relative to the DMSO control values at 2 hr and plotted as the mean ± s.e.m. (n = 3). *, $P < 0.05$; **, $P < 0.01$; ***, $P < 0.001$, determined by Student's *t* test using Nutlin-3a and Nutlin-3a + NVP-2 (B), 5-FUR and 5-FUR + NVP-2 (C), 5-FdUR and 5-FdUR + NVP-2 (D), Nutlin-3a and Nutlin-3a + DT-061 (E), and 5-FU and 5-FU + DT-061 (F) data sets.